

Nebular emission-line profiles of Type Ib/c Supernovae – probing the ejecta asphericity.

S. Taubenberger¹*, S. Valenti^{2,3}, S. Benetti⁴, E. Cappellaro⁴, M. Della Valle⁵, N. Elias-Rosa^{1,6}, S. Hachinger¹, W. Hillebrandt¹, K. Maeda^{1,7}, P. A. Mazzali^{1,4}, A. Pastorello³, F. Patat², S. A. Sim¹ and M. Turatto⁸

¹Max-Planck-Institut für Astrophysik, Karl-Schwarzschild-Str. 1, 85741 Garching bei München, Germany

²European Southern Observatory (ESO), Karl-Schwarzschild-Str. 2, 85748 Garching bei München, Germany

³Astrophysics Research Centre, School of Mathematics and Physics, Queen's University Belfast, Belfast BT7 1NN, UK

⁴INAF Osservatorio Astronomico di Padova, Vicolo dell'Osservatorio 5, 35122 Padova, Italy

⁵INAF Osservatorio Astronomico di Capodimonte, Via Moiariello 16, 80131 Napoli, Italy

⁶Spitzer Science Center, California Institute of Technology, 1200 E. California Blvd., Pasadena, CA 91125, USA

⁷Institute for the Physics and Mathematics of the Universe, Univ. of Tokyo, Kashiwanoha 5-1-5, Chiba-ken 277-8582, Japan

⁸INAF Osservatorio Astrofisico di Catania, Via S.Sofia 78, 95123 Catania, Italy

In original form 2008 October 1

ABSTRACT

In order to assess qualitatively the ejecta geometry of stripped-envelope core-collapse supernovae, we investigate 98 late-time spectra of 39 objects, many of them previously unpublished. We perform a Gauss-fitting of the [O I] $\lambda\lambda 6300, 6364$ feature in all spectra, with the position, full width at half maximum (FWHM) and intensity of the $\lambda 6300$ Gaussian as free parameters, and the $\lambda 6364$ Gaussian added appropriately to account for the doublet nature of the [O I] feature. On the basis of the best-fit parameters, the objects are organised into morphological classes, and we conclude that at least half of all Type Ib/c supernovae must be aspherical. Bipolar jet-models do not seem to be universally applicable, as we find too few symmetric double-peaked [O I] profiles. In some objects the [O I] line exhibits a variety of shifted secondary peaks or shoulders, interpreted as blobs of matter ejected at high velocity and possibly accompanied by neutron-star kicks to assure momentum conservation. At phases earlier than ~ 200 d, a systematic blueshift of the [O I] $\lambda\lambda 6300, 6364$ line centroids can be discerned. Residual opacity provides the most convincing explanation of this phenomenon, photons emitted on the rear side of the SN being scattered or absorbed on their way through the ejecta. Once modified to account for the doublet nature of the oxygen feature, the profile of Mg I $\lambda 4571$ at sufficiently late phases generally resembles that of [O I] $\lambda\lambda 6300, 6364$, suggesting negligible contamination from other lines and confirming that O and Mg are similarly distributed within the ejecta.

Key words: supernovae: general – techniques: spectroscopic – line: profile

1 INTRODUCTION

The geometry of stripped-envelope core-collapse supernova (CC-SN) ejecta has been scrutinised for about ten years, since the association of SN 1998bw with the nearby γ -ray burst GRB 980425 (Galama et al. 1998). Together with subsequent examples of SN-GRB associations (see e.g. Ferrero et al. 2006 for an overview) this suggested that at least some Type Ib/c supernovae (SNe Ib/c) may be powered by the same engine as long-duration GRBs, and thus

that their ejecta may show large-scale asphericity along an axis defined by the GRB-jet. Indeed, the nebular spectra of SN 1998bw exhibited properties which could not be explained with spherical symmetry (Mazzali et al. 2001; Maeda et al. 2002). Instead, a model with high-velocity Fe-rich material ejected along the jet axis, and lower-velocity O in a torus perpendicular to this axis, was proposed. From this geometry a strong viewing-angle dependence of nebular line profiles was obtained (Maeda et al. 2002). Of particular note to this study, this model suggests that double-peaked O lines should be observed if viewed from a direction perpendicular to the jet.

* E-mail: tauben@mpa-garching.mpg.de

Such a profile was first observed in SN 2003jd (Mazzali et al. 2005), an important step towards a coherent picture. However, whether large-scale asphericity is found only in SNe Ic connected with a GRB (probably only a few percent of all SNe Ic; Podsiadlowski et al. 2004; Guetta & Della Valle 2007), and how large the degree of asphericity in ‘normal’ SNe Ib/c actually is, are debated. Maeda et al. (2008) recently studied a sample of nebular spectra of 18 stripped-envelope CC-SNe and found a large fraction of double-peaked [O I] $\lambda\lambda 6300, 6364$ line profiles, consistent with about half of all SNe Ib/c being strongly, or all of them moderately, aspherical. Similarly, Modjaz et al. (2008) analysed late-time spectra of 8 stripped CC-SNe, concluding that asphericity is ubiquitous in all these events, not only the hyperenergetic ones. It should be noted that the Maeda et al. and Modjaz et al. works focus on deviations from sphericity on *global* scales, as opposed to small-scale clumpiness of the ejecta that results in fine-structured emission lines and requires fairly high-resolution nebular spectra to be studied (see e.g. Filippenko & Sargent 1989; Spyromilio 1994; Matheson et al. 2000).

In this work we conduct a study similar to that of Maeda et al. (2008) and Modjaz et al. (2008), but based on a larger sample of SNe, considering virtually all nebular SN Ib/c spectra we could access from the literature, complemented by 26 previously unpublished spectra from the Asiago Supernova Archive and recent observations carried out at the ESO Very Large Telescope (VLT). The work is organised as follows: in Section 2 we present the entire SN sample, discuss the selection criteria for spectra to be included, and discuss in more detail those spectra which were previously unpublished. Section 3 concentrates on the link between the ejecta geometry and observed line profiles, motivates the choice to focus on [O I] $\lambda\lambda 6300, 6364$, addresses the complications arising from its doublet nature, and introduces the fitting procedure employed to gain qualitative insight into the ejecta morphology. The results of this fitting are analysed in Sections 4 and 5, trying to find an explanation for the mean blueshifts of the line’s centroids at phases $\lesssim 200$ d, and dividing the objects into different classes on the basis of the best-fit parameters. Individual objects with interesting line profiles are discussed more deeply in Section 6, while Section 7 extends the analysis to the profile of Mg I $\lambda 4571$ and its comparison to that of [O I]. Finally, a brief summary of the main results is given in Section 8.

2 THE SAMPLE OF SN Ib/c SPECTRA

Our goal is to compare a large set of late-time spectra of stripped-envelope CC-SNe, concentrating on what can be learned about the ejecta geometry by studying the profiles of nebular emission lines, in particular [O I] $\lambda\lambda 6300, 6364$ (the motivation to focus on this line is given in Section 3).

Given the statistical approach of this study, we use a simple fitting procedure (for details see Section 3). Compared to full spectral modelling this method has the advantage of being fast, capable of dealing with complex profiles, and independent of an accurate flux calibration of the spectra, thus allowing it to be applied to a large number of spectra.

Nebular emission features in SNe Ib/c typically start

to emerge about two months past maximum light, but at that epoch the SN flux is still dominated by photospheric emission. For this reason we included in our sample only spectra which were taken more than ~ 90 d after maximum light, which, assuming typical rise times, corresponds to 100 or 110 d after explosion. At those phases there still is an underlying photospheric continuum, but this should not affect severely the profiles of forbidden emission lines, so that they can be used to trace the geometry of the ejecta (but see Section 4 for the consequence of residual optical depth). Maeda et al. (2008) employed a more stringent criterion, restricting their sample to spectra with epochs ≥ 200 d to avoid any possible deformation of lines by optical-depth effects. This criterion would reduce our sample from 98 to 53 spectra (including 16 SNe not analysed by Maeda et al.), and deprive us of the possibility to investigate when the ejecta become fully transparent, which is addressed in Section 4.

Applying a phase cut required a fairly precise estimate of the epoch of explosion or maximum light. Whenever a complete light curve was not available, this information was reconstructed from discovery and classification remarks reported in IAU-circulars. In exception to this rule, spectra of three SNe were included for which no early observations exist. However, the spectrum of SN 1995bb (Matheson et al. 2001) is decidedly nebular, as are the later two out of three spectra of SN 1990aj. The first one in this series appears rather peculiar and may still show some photospheric features, but was included for completeness. Finally, a spectrum of SN 2005N was dated to ~ 90 d past maximum light by cross-correlation with a set of comparison spectra (Harutyunyan et al. 2008). Besides the constraints on the phase, also spectra with insufficient signal-to-noise ratio (S/N) in the wavelength region of interest were rejected.

2.1 The full sample

The full catalogue of spectra studied in this work is presented in Table 1, complemented by additional information on the SN classifications and host-galaxy properties.

2.2 Previously unpublished spectra

Our sample contains 26 nebular spectra of 17 SNe Ib/c not previously published elsewhere. Another 4 spectra of the Asiago archive were shown by Turatto (2003) and Valenti et al. (2008) before. Most of these spectra were taken in the course of the ESO-Asiago SN monitoring programme in the 1990s (Turatto 2000) using the ESO - La Silla 3.6m (equipped with EFOSC / EFOSC2), 2.2m (+ EFOSC2) and 1.5m (+ Boller & Chivens spectrograph) Telescopes and the 1.54m Danish Telescope (equipped with DFOSC). From 2004 onwards, several spectra were acquired through dedicated VLT programmes (VLT-U1 equipped with FORS2). The set is complemented by single spectra taken with the Siding Spring 2.3m Telescope (+ double-beam spectrograph) and the Nordic Optical Telescope (+ ALFOSC). Details on the dates of the observations and the instrumental setup are summarised in Table 2.

Applying the selection criteria mentioned above, our full sample consists of 39 SNe with 98 nebular spectra. It contains almost all suitable spectra up to the

Table 1. List of SNe Ib/c included in the sample – 1st part.

SN	Type	Host galaxy	Morphology ^a	v_{rec}^b	Redshift	Date	Epoch ^c	Reference
1983N	Ib	NGC 5236	SBC	554 ± 119	0.0018(04)	1984/03/01	226 ± 5	Gaskell et al. 1986
1985F	Ib/c	NGC 4618	SBm	544 ± 59	0.0018(02)	1985/03/19	280 ± 4	Filippenko & Sargent 1986
1987M	Ic	NGC 2715	SABc	1216 ± 132	0.0041(04)	1988/02/09	141 ± 7	Filippenko et al. 1990
						1988/02/25	157 ± 7	Filippenko et al. 1990
1988L	Ic	NGC 5480	Sc	1963 ± 100	0.0065(03)	1988/07/17	90 ± 12	Matheson et al. 2001
						1988/09/15	149 ± 12	Matheson et al. 2001
1990B	Ic	NGC 4568	Sbc(M)	2255 ± 153	0.0075(05)	1990/04/19	91 ± 2	Clocchiatti et al. 2001
						1990/04/30	102 ± 2	Matheson et al. 2001
1990I	Ib	NGC 4650A	S0/a(M)	2880 ± 99^d	0.0096(03)	1990/07/26	90 ± 2	Elmhamdi et al. 2004
						1990/12/21	237 ± 2	Elmhamdi et al. 2004
						1991/02/20	298 ± 2	Elmhamdi et al. 2004
1990U	Ic	NGC 7479	SBbc	2525 ± 162	0.0084(05)	1990/10/20	100 ± 12	Matheson et al. 2001
						1990/10/24	104 ± 12	Gómez & López 1994
						1990/11/23	134 ± 12	Asiago archive
						1990/11/28	139 ± 12	Matheson et al. 2001
						1990/12/12	153 ± 12	Matheson et al. 2001
						1990/12/20	161 ± 12	Asiago archive
						1991/01/06	178 ± 12	Matheson et al. 2001
						1991/01/12	184 ± 12	Gómez & López 1994
1990W	Ib/c	NGC 6221	SBC	1481 ± 126	0.0049(04)	1991/02/21	183 ± 3	Asiago archive
						1991/04/21	242 ± 3	Asiago archive
1990aa	Ic	MCG+05-03-016	Sb	5032 ± 108	0.0168(04)	1991/01/12	130 ± 7	Gómez & López 2002
						1991/01/23	141 ± 7	Matheson et al. 2001
1990aj	Ib/c _{pec}	NGC 1640	SBb(R)	1604 ± 64^d	0.0053(02)	1991/01/29	140 ± 50	Asiago archive
						1991/02/22	164 ± 50	Asiago archive
						1991/03/10	180 ± 50	Matheson et al. 2001
1991A	Ic	IC 2973	SBcd	3232 ± 84	0.0107(03)	1991/03/22	99 ± 10	Gómez & López 1994
						1991/04/07	115 ± 10	Matheson et al. 2001
						1991/04/16	124 ± 10	Gómez & López 1994
						1991/06/08	177 ± 10	Gómez & López 1994
1991L	Ib/c	MCG+07-34-134	Sc(M)	9186 ± 200^d	0.0306(07)	1991/06/08	121 ± 20	Gómez & López 2002
1991N	Ic	NGC 3310	SABb(R)	1071 ± 80	0.0036(03)	1991/12/14	274 ± 15	Matheson et al. 2001
						1992/01/09	300 ± 15	Matheson et al. 2001
1993J	I Ib	NGC 3031	Sab	-140 ± 192^d	-0.0001(06)	1993/10/19	205 ± 3	Barbon et al. 1995
						1993/11/19	236 ± 3	Barbon et al. 1995
						1993/12/08	255 ± 3	Barbon et al. 1995
						1994/01/17	295 ± 3	Barbon et al. 1995
						1994/01/21	299 ± 3	Barbon et al. 1995
						1994/01/22	300 ± 3	Barbon et al. 1995
						1994/03/25	362 ± 3	Barbon et al. 1995
						1994/03/30	367 ± 3	Barbon et al. 1995
1994I	Ic	NGC 5194	Sbc(M)	493 ± 70	0.0016(02)	1994/07/14	97 ± 1	Filippenko et al. 1995
						1994/08/04	118 ± 1	Filippenko et al. 1995
						1994/09/02	147 ± 1	Filippenko et al. 1995
1995bb	Ib/c	anonymous	S/Irr	1626 ± 250	0.0054(08)	1995/12/17	nebular	Matheson et al. 2001
1996D	Ic	NGC 1614	SBC(M)	4531 ± 167	0.0151(06)	1996/09/10	214 ± 10	Asiago archive
1996N	Ib	NGC 1398	SBab(R)	1396 ± 214	0.0047(07)	1996/10/19	224 ± 7	Sollerman et al. 1998
						1996/12/16	282 ± 7	Sollerman et al. 1998
						1997/01/13	310 ± 7	Sollerman et al. 1998
						1997/02/12	340 ± 7	Sollerman et al. 1998
1996aq	Ib	NGC 5584	SABc	1675 ± 83	0.0056(03)	1997/02/11	176 ± 4	Asiago archive
						1997/04/02	226 ± 4	Asiago archive
						1997/05/14	268 ± 4	Asiago archive
1997B	Ic	IC 438	SABc(R)	2919 ± 144	0.0097(05)	1997/09/23	262 ± 5	Asiago archive
						1997/10/11	280 ± 5	Asiago archive
						1998/02/02	394 ± 5	Asiago archive
1997X	Ic	NGC 4691	SB0/a	1072 ± 47	0.0036(02)	1997/05/10	103 ± 5	Gómez & López 2002
						1997/05/13	106 ± 5	Asiago archive
1997dq	Ic	NGC 3810	Sc	993 ± 114^d	0.0033(04)	1998/05/30	217 ± 10	Asiago archive
						1998/06/18	236 ± 10	Matheson et al. 2001
1997ef	BL-Ic	UGC 4107	Sc	3452 ± 63	0.0115(02)	1998/09/21	287 ± 3	Matheson et al. 2001
1998bw	BL-Ic	ESO184-G82	SBbc	2445 ± 135	0.0082(05)	1998/09/12	126 ± 1	Patat et al. 2001
						1998/11/26	201 ± 1	Patat et al. 2001
						1999/04/12	337 ± 1	Patat et al. 2001
						1999/05/21	376 ± 1	Patat et al. 2001
1999cn	Ic	MCG+02-38-043	Sab	6502 ± 235	0.0217(08)	2000/04/08	297 ± 5	Asiago archive
1999dn	Ib	NGC 7714	SBb(M)	2744 ± 74	0.0091(02)	2000/09/01	375 ± 5	Asiago archive

year 2004 that could be retrieved from the literature, complemented by previously unpublished spectra from the Asiago Supernova Archive (Barbon et al. 1993, <http://web.oapd.inaf.it/supern/cat/>) and selected spectra obtained through dedicated programmes after 2004. The observations thus span the entire era of SN CCD spectroscopy.

Spectra from the Asiago and MPA archives are presented in Fig. 1. They have been optimally extracted (Horne 1986) using standard tasks in IRAF¹ or MIDAS, wavelength

¹ IRAF is distributed by the National Optical Astronomy Observatories, which are operated by the Association of Universities

Table 1. *continued.* List of SNe Ib/c included in the sample – 2nd part.

SN	Type	Host galaxy	Morphology ^a	v_{rec}^b	Redshift	Date	Epoch ^c	Reference
2000ew	Ic	NGC 3810	Sc	1049 ± 114	0.0035(04)	2001/03/17	112 ± 12	Asiago archive
2002ap	BL-Ic	NGC 628	Sc	657 ± 22^d	0.0022(01)	2002/06/09	123 ± 1	Foley et al. 2003
						2002/06/18	132 ± 1	Foley et al. 2003
						2002/07/12	156 ± 1	Foley et al. 2003
						2002/08/09	185 ± 1	Foley et al. 2003
						2002/10/01	237 ± 1	Foley et al. 2003
						2002/10/09	245 ± 1	Foley et al. 2003
						2002/10/14	250 ± 1	SSO / Asiago archive
						2002/11/06	274 ± 1	Foley et al. 2003
						2003/01/07	336 ± 1	Foley et al. 2003
						2003/02/27	386 ± 1	Foley et al. 2003
2003jd	BL-Ic	MCG-01-59-021	SABm	5654 ± 78	0.0188(03)	2004/09/11	317 ± 1	Mazzali et al. 2005
						2004/10/18	354 ± 1	Mazzali et al. 2005
2004aw	Ic	NGC 3997	SBb(M)	4900 ± 118	0.0163(04)	2004/11/14	236 ± 1	Taubenberger et al. 2006
						2004/12/08	260 ± 1	Taubenberger et al. 2006
						2005/05/11	413 ± 1	Taubenberger et al. 2006
2004gt	Ic	NGC 4038	SBm(M)	1424 ± 133	0.0047(04)	2005/05/24	160 ± 5	Asiago archive
2005N	Ib/c	NGC 5420	Sb	4885 ± 198^d	0.0163(07)	2005/01/21	88 ± 30	Harutyunyan et al. 2008
2006F	Ib	NGC 935	Sc(M)	4270 ± 180	0.0142(06)	2006/11/16	312 ± 7	Maeda et al. 2008
2006T	IIB	NGC 3054	SBb(R)	2560 ± 182	0.0085(06)	2007/02/18	371 ± 2	Maeda et al. 2008
2006aj	BL-Ic	anonymous	late spiral	9845 ± 250	0.0328(08)	2006/09/19	204 ± 1	Mazzali et al. 2007a
						2006/11/27	273 ± 1	MPA data base
						2006/12/19	295 ± 1	MPA data base
2006gi	Ic	NGC 3147	Sbc	2820 ± 178^d	0.0094(06)	2007/02/10	148 ± 5	Asiago archive
2006ld	Ib	UGC 348	SABd(R)	4168 ± 41	0.0139(01)	2007/07/17	280 ± 4	MPA data base
						2007/08/06	300 ± 4	MPA data base
						2007/08/20	314 ± 4	MPA data base
2007C	Ib	NGC 4981	SBbc(R)	1766 ± 116	0.0059(04)	2007/05/17	131 ± 4	MPA data base
						2007/06/20	165 ± 4	MPA data base
2007I	BL-Ic	anonymous	late spiral	6445 ± 250	0.0215(08)	2007/06/18	165 ± 6	MPA data base
						2007/07/15	192 ± 6	MPA data base

^a Classification according to LEDA (Lyon-Meudon Extragalactic Database, <http://leda.univ-lyon1.fr/>).^b Recession velocity in km s^{-1} , inferred from narrow H α ; error from ‘vmaxg’ (LEDA).^c Epoch in days from *B*-band maximum light; photometry of SN 1985F from Tsvetkov (1986).^d No H α visible; heliocentric host-galaxy recession velocity from NED (NASA/IPAC Extragalactic Database, <http://nedwww.ipac.caltech.edu/>) used.

calibrated with respect to arc lamps, and flux calibrated using instrumental response curves obtained from spectrophotometric standard stars observed in the same nights. However, no attempt has been made to calibrate the fluxes to a proper absolute scale through a comparison to contemporaneous photometry.

The spectra all show [O I] $\lambda\lambda 6300, 6364$ as one of their strongest features, complemented by other lines typical of SNe Ib/c at late phases, most notably [Ca II] $\lambda\lambda 7291, 7323$ / [O II] $\lambda\lambda 7320, 7330$, Mg I $\lambda 4571$, a multitude of blended [Fe II] lines around 5000 Å, and the near-IR Ca II triplet. In spectra taken less than 150 d after maximum a contribution from photospheric lines and a weak pseudo-continuum can be discerned. Some spectra also show evidence of an underlying stellar continuum caused by an imperfect host-galaxy subtraction.

3 FITTING THE OXYGEN LINE

[O I] $\lambda\lambda 6300, 6364$ is one of the dominant features of nebular spectra of stripped-envelope CC-SNe, and the most useful to study the ejecta geometry, in particular the degree of asphericity. Compared to the multitude of forbidden Fe lines found mostly at bluer wavelength and to the [Ca II] / [O II] feature around 7300 Å, the [O I] $\lambda\lambda 6300, 6364$ doublet is

largely isolated and unblended. In contrast to the weaker Mg I $\lambda 4571$ it lies in a region which is covered by almost all late-time spectra, and where the sensitivity of most spectrographs is at its maximum, allowing for relatively good S/N. Furthermore, oxygen is the most abundant element in the ejecta of stripped-envelope CC-SNe, thus telling more about the overall geometry than the distribution of a minor species like Ca.

In this section we describe our method to obtain constraints on the geometry of the ejected oxygen, which involves the characterisation of the expected line profile, the development of a suitable parametrisation, and the actual procedure applied to infer the best-fitting parameters for each spectrum.

3.1 Line profiles

In completely transparent SN ejecta the profile of a forbidden emission line traces the emissivity in this line, which in turn is determined by the spatial distributions and velocity fields of both the emitting species and ⁵⁶Co, whose radioactive decay provides the energy to excite the line’s upper level (Fransson & Chevalier 1987, 1989). In SNe Ic the O- and Co-rich parts represent a significant fraction of the entire ejecta, and the [O I] feature traces a substantial amount of material. Thanks to homologous expansion ($r = vt$), the profile of the [O I] emission line is a 1D line-of-sight projection of the 3D oxygen emissivity distribution.

In this work, we fit the oxygen feature with a Gaus-

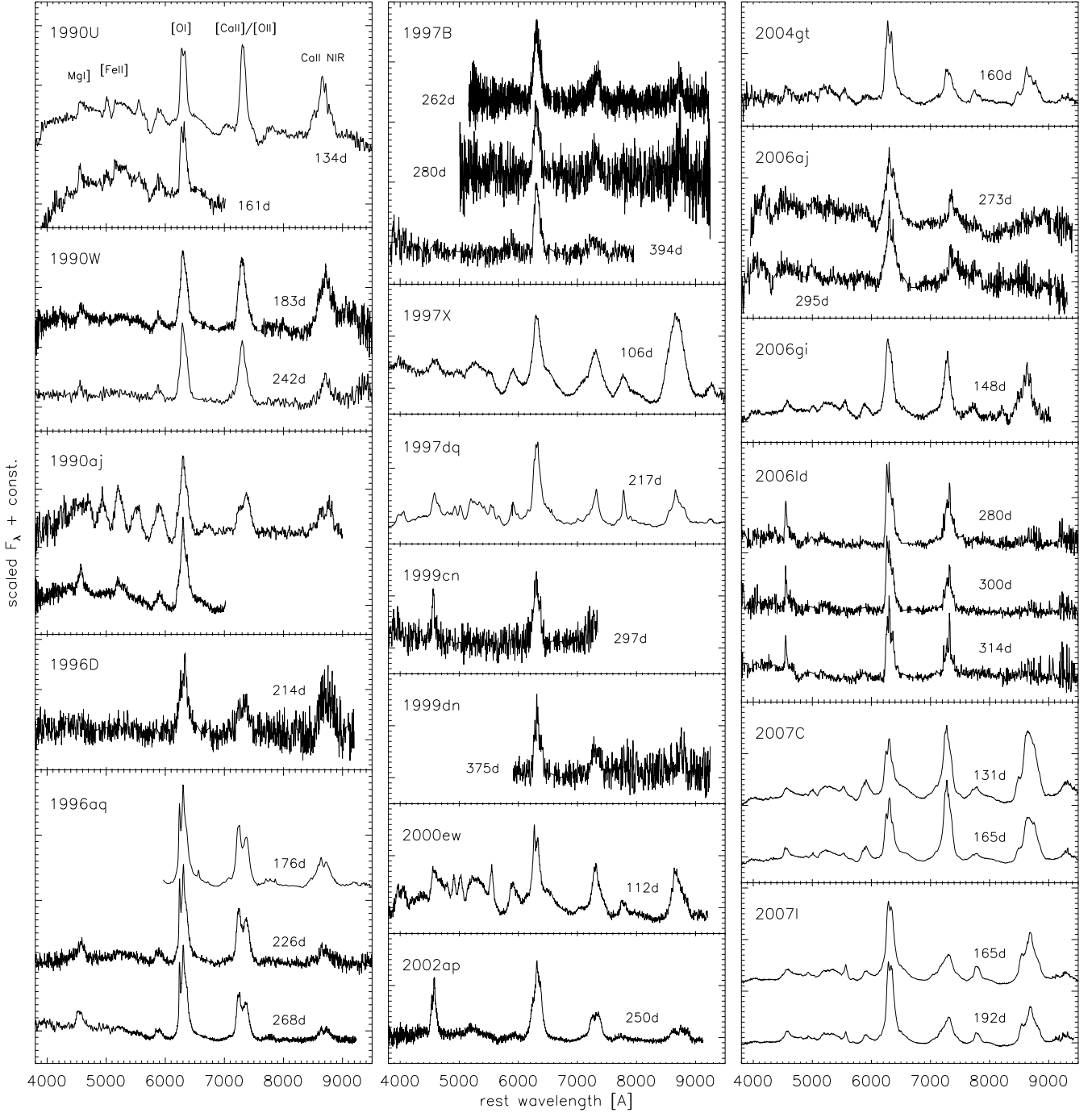


Figure 1. Spectra from the Asiago archive and the MPA data base, most of them previously unpublished (cf. Table 2). All spectra are shown at their rest wavelength inferred (whenever possible) from narrow interstellar H α lines. Overly strong continuum slopes and narrow host-galaxy emission features have been removed for presentation purposes, and the spectra have been scaled and vertically displaced by arbitrary amounts. The major features are labelled in the first spectrum.

sian or – for SNe with more complex line profiles – with a superposition of multiple Gaussians. This provides at least qualitative information on the distribution (through the position and strength of the various components) and radial extent (through the components' FWHM) of excited oxygen in the SN ejecta. However, a full restoration of the 3D density distribution is not attempted, since the solution is highly degenerate.

3.2 [O I] λ 6300 and [O I] λ 6364

As mentioned above, an advantage of the oxygen feature is its isolated position, unblended with lines from other elements. However, the feature itself is a doublet of [O I] λ 6300 and [O I] λ 6364, both forbidden M1 transitions which share the same upper level ($^3P_{1,2} - ^1D_2$). The intensity ratio of these two lines depends on the ambient O I den-

Table 2. Instrumental details of spectra from the Asiago archive and the MPA data base.

SN	Date	Instrumental setup
1990U	1990/11/23	ESO 3.6m + EFOSC + B300 + R300
	1990/12/20	ESO 3.6m + EFOSC + B300
1990W	1991/02/21	ESO 3.6m + EFOSC + B300 + R300
	1991/04/21	ESO 3.6m + EFOSC + B300 + R300
1990aj	1991/01/29 ^a	ESO 2.2m + EFOSC2 + gr1
	1991/02/22 ^a	ESO 3.6m + EFOSC + B300 + R300
1996D	1996/09/10	ESO 1.5m + B&C + gt15
1996aq	1997/02/11	ESO 3.6m + EFOSC + R300
	1997/04/02 ^b	ESO 1.5m + B&C + gt15
	1997/05/14	ESO 2.2m + EFOSC2 + gr1 + gr5
1997B	1997/09/23	ESO 2.2m + EFOSC2 + gm5
	1997/10/11	Danish 1.54m + DFOSC + gr5
	1998/02/02 ^a	ESO 3.6m + EFOSC2 + gr6
1997X	1997/05/13	ESO 2.2m + EFOSC2 + gr1 + gr5
1997dq	1998/05/30	ESO 3.6m + EFOSC2 + B300N + R300N
1999cn	2000/04/08	ESO 3.6m + EFOSC2 + gr11
1999dn	2000/09/01	ESO 3.6m + EFOSC2 + gr12
2000ew	2001/03/17	Danish 1.54m + DFOSC + gm4
2002ap	2002/10/14	SSO 2.3m + DBS
2004gt	2005/05/24	VLT-U1 + FORS2 + 300V
2006aj	2006/11/27	VLT-U1 + FORS2 + 300V + 300I
	2006/12/19	VLT-U1 + FORS2 + 300V
2006gi	2007/02/10	NOT 2.56m + ALFOSC + gm4
2006ld	2007/07/17	VLT-U1 + FORS2 + 300V
	2007/08/06	VLT-U1 + FORS2 + 300V
	2007/08/20	VLT-U1 + FORS2 + 300V
2007C	2007/05/17	VLT-U1 + FORS2 + 300V
	2007/06/20	VLT-U1 + FORS2 + 300V + 300I
2007I	2007/06/18	VLT-U1 + FORS2 + 300V + 300I
	2007/07/15	VLT-U1 + FORS2 + 300V

^a Already shown by Turatto (2003).^b Already shown by Valenti et al. (2008).

sity, and can vary from 1:1 to 3:1 depending on the environmental conditions. The transition between the asymptotic values occurs at O I densities of $n(\text{O I}) \approx 10^{10} \text{ cm}^{-3}$. This fact has been theoretically derived by Li & McCray (1992) and Chugai (1992), and observationally confirmed by Phillips & Williams (1991) and Spyromilio & Pinto (1991) for SN 1987A, Leibundgut et al. (1991) for SN 1986J, and Spyromilio (1991) for SN 1988A.

Compared to the aforementioned SNe II, the stripped CC-SNe of our sample show larger ejecta velocities. While Spyromilio & Pinto (1991) measured a FWHM of 2800 km s^{-1} for the [O I] line in SN 1987A, the SNe discussed here have FWHM of $\sim 6000 \text{ km s}^{-1}$. Assuming a Gaussian density profile with 6000 km s^{-1} FWHM and $1M_{\odot}$ of neutral oxygen homogeneously distributed within the ejecta, the central O I density would have dropped to $4\text{--}5 \times 10^8 \text{ cm}^{-3}$ by 100 d, an order of magnitude below the density where deviations from a 3:1 line ratio become apparent. Even if the oxygen was clumped on small scales within an overall Gaussian profile [as in SN 1987A, for which Spyromilio & Pinto (1991) suggested an oxygen filling factor of $\sim 10\%$ based on the observed evolution of the [O I] ratio], ratios significantly different from 3:1 would only be encountered for very small filling factors ($< 10\%$). We therefore adopt the low-density limit (3:1) for all spectra, noting that possible small deviations at the earliest epochs do not severely affect any of our basic conclusions.

With this choice, it is sufficient to specify the amplitude, central wavelength and FWHM of the $\lambda 6300$ line. The parameters for the $\lambda 6364$ line are then forced. Hereafter we

refer to such a set of three parameters as *one component* of the fit to the [O I] profile; up to three such components were employed to obtain good fits.

3.3 The fitting procedure

The actual fitting was accomplished using the IRAF task NFIT1D, which is part of the STSDAS package. A user-defined fitting-function was introduced, which consisted of up to three components, as defined above.

The background level was determined by eye on both sides of the [O I] feature and interpolated linearly to account for a possible underlying continuum formed by residual photospheric lines or a contamination by star light. Since the background parameters are determined from a different wavelength region than the line parameters, the background fit is technically decoupled from the line fit, although of course the best-fit line parameters may be affected by the choice of the background. This can be problematic in relatively early spectra (up to ~ 150 d), where underlying photospheric lines are present, and the local continuum is more strongly inclined than at later times. However, tests with different choices of the continuum level have shown that the uncertainty introduced e.g. in the central wavelength of the line is $\lesssim 5 \text{ \AA}$ even in cases with very complex background. More typical uncertainties are $\lesssim 2 \text{ \AA}$ and thus smaller than the uncertainties in the wavelength calibration and redshift correction of most spectra.

For the up-to-nine parameters of the line fit (amplitude, position λ and FWHM of up-to-three components) the main difficulty consisted in identifying the global minimum for a given number of components. Therefore, for fits with two or three components, a refined two-step fitting procedure was applied to avoid local minima. First, a set of synthetic line profiles were generated, changing all parameters by equidistant steps over a fairly wide range. The resulting profiles were compared to the observed ones, and the one with minimum RMS was identified. In a second step the values thus derived were used as initial guesses for NFIT1D, ensuring that the fit converged to the global minimum. We always started the fitting with one component. Other components were added only if the fit residuals strongly exceeded the noise level of the spectrum.

The best-fitting values for single- and double-component fits to all spectra are reported in Appendix A (Table A1), while the parameters of three-component fits to individual spectra are given in Table A2. In these tables and during the further discussion, we define α_i as the integrated flux of the i -th component of the fit, normalised to the total integrated flux of the oxygen feature. The best fits are compared with the observed line profiles in Fig. 2.

4 BLUESHIFTED LINE CENTROIDS AT EARLY PHASES

In Fig. 3 we plot the position of the $\lambda 6300$ -Gaussian in the one-component fits against the epoch of the spectra. The position should be a fair tracer of the actual line centroid. The scatter of the data points arises from the peculiarities of individual objects and uncertainties in their redshifts.

However, on top of this scatter Fig. 3 shows that there

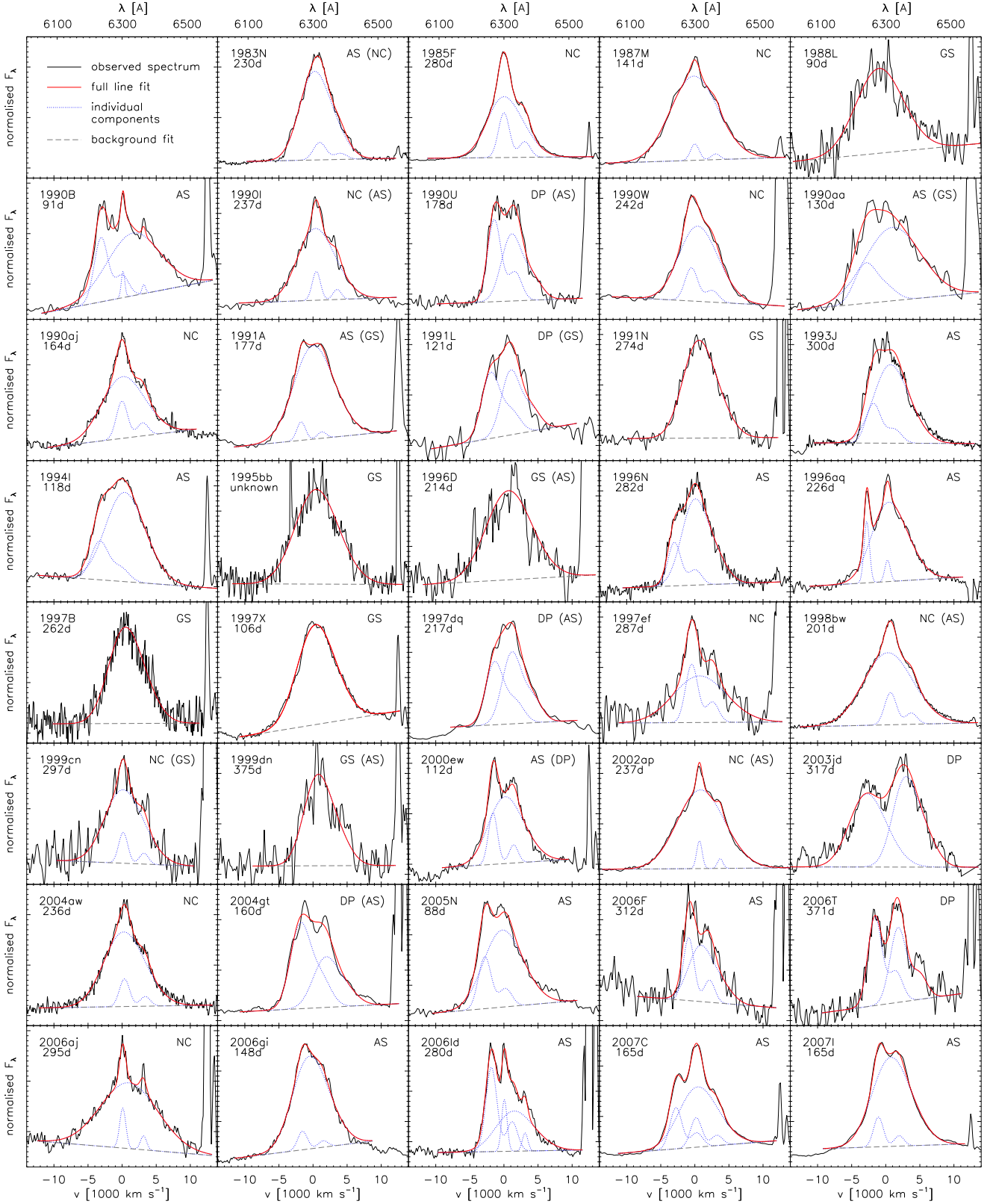


Figure 2. Observed [O I] $\lambda\lambda 6300, 6364$ features in the spectra of our sample (solid black lines) with multi-Gaussian fits (Tables A1 and A2) overplotted (solid red lines). Individual components are overplotted as dotted blue lines, and the adopted linear background levels are indicated by dashed grey lines. H α was subtracted from the spectrum of SN 1993J (cf. Table A1). The different line categories as defined in Section 5.1 are labelled as follows: GS for Gaussian, NC for narrow core, DP for double peak, AS for asymmetric / multi-peaked (alternative classifications are given in brackets). Only one spectrum of each object is included in the figure.

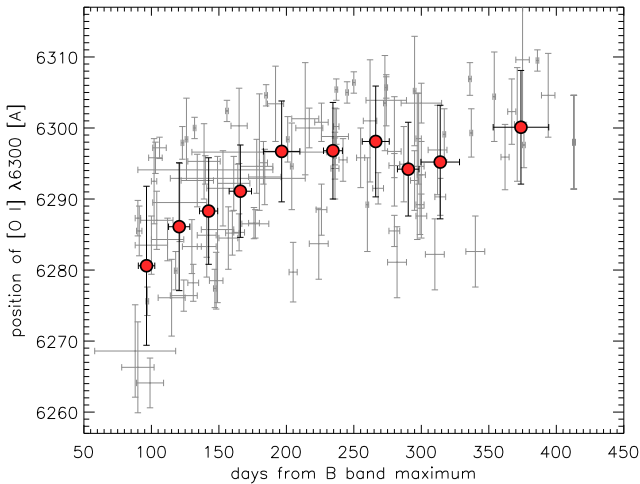


Figure 3. [O I] $\lambda 6300$ line centroids (as inferred from the position of the $\lambda 6300$ Gaussian in one-component fits), plotted vs. the epochs of the spectra with respect to B -band maximum. The filled circles represent bins of 10 spectra. A systematic blueshift can be discerned at epochs earlier than 200 d.

is a systematic trend of the [O I] feature being blueshifted in spectra taken earlier than ~ 200 d past maximum, and the effect is stronger the earlier the phase. In the spectra taken around 100 d, the average blueshift is ~ 20 Å, corresponding to ~ 1000 km s $^{-1}$. In the following, possible interpretations of the observed effect are discussed, and their suitability to explain the observations is considered.

(i) *Ejecta geometry.* Line shifts such as those observed in [O I] could, in principle, arise from a one-sided ejecta geometry, caused for instance by low-mode convective instabilities (Scheck et al. 2004, 2006; Kifonidis et al. 2006) or the Standing Accretion Shock Instability (SASI; Blondin et al. 2003). However, this can *not* explain the decrease of the shifts with time. Moreover, there is no reason why particular ejecta geometries should result in a systematic *blueshift* of the line centroid, as different spatial orientations should occur in the observed sample. Note that relativistic forward boosting is irrelevant at the observed ejecta velocities (no more than ~ 8000 km s $^{-1}$, even in the extreme line wings).

(ii) *Dust formation.* As the SN ejecta expand and cool, the temperature eventually drops below the threshold where dust can form. Consequently, the light from the far side of the ejecta is partly absorbed, resulting in the suppression of the redshifted part of emission lines. This effect has been observed in some Type II SNe, for instance SNe 1987A and 1999em, more than one year after explosion (cf. e.g. Danziger et al. 1989, Lucy et al. 1989 and Elmhamdi et al. 2003). In ordinary SNe Ib/c dust formation has never been unambiguously detected at a few hundred days (e.g., Sollerman, Leibundgut & Spyromilio 1998, Matheson et al. 2000 and Elmhamdi et al. 2004; but see also Matthews et al. 2002). Moreover, dust formation (if present) should manifest itself in a line blueshift *increasing* with time, the opposite of what we see in our sample, and hence cannot be a suitable explanation for our observations.

(iii) *Contamination from other emission lines.* In principle, other lines blended into the blue wing of [O I] $\lambda\lambda 6300, 6364$ could generate the observed blueshift of this

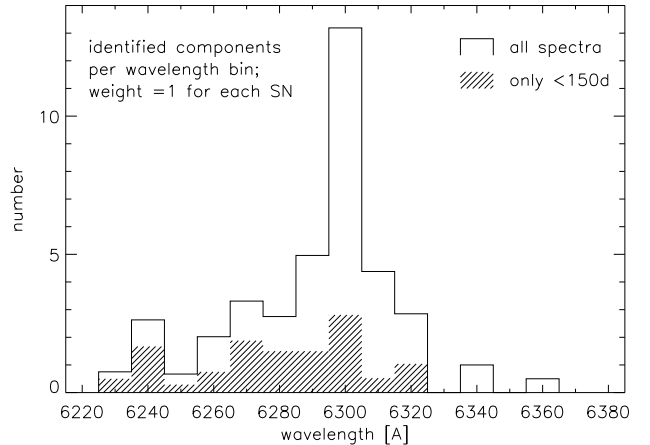


Figure 4. Histogram of components identified in the spectra with our Gaussian fitting procedure (wavelengths refer to [O I] $\lambda 6300$; cf. Tables A1, A2 and Fig. 2). To give equal weight to all SNe, the numbers have been rescaled such that every SN yields a contribution equivalent to one component (hence the fractional numbers). The empty histogram refers to the full sample, the shaded region to a subsample of spectra taken earlier than 150 d after maximum.

feature. At early epochs, when a strong blueshift is observed, the contamination could e.g. arise from residual emission of permitted photospheric lines. The biggest problem with this idea is the apparent lack of suitable candidates. Elmhamdi et al. (2004) suggested a contribution of Fe II $\lambda 6239$ in SN 1990I around +90 d, but this is not expected to be a particularly strong line, and it is unclear why it should be so prominent while other, intrinsically stronger Fe lines are not. Moreover, a histogram of fit components (Fig. 4) does not show evidence of a distinct additional line at a wavelength shorter than 6300 Å. Instead, in the subsample of spectra taken at < 150 d (shaded area in Fig. 4), the distribution of fit components smoothly smears out to shorter wavelengths. Finally, in Section 7 we will show that the profile of Mg I $\lambda 4571$ is similar to that of [O I] $\lambda 6300$ in a majority of our spectra (also those with blueshifted lines), and an identical contamination in both lines is very unlikely.

(iv) *Opaque inner ejecta.* The failure of other explanations and the characteristics of the fit-component histogram leave us with residual opacity in the core of the ejecta as a possible explanation for the observed blueshift (Chugai 1992; Wang & Hu 1994). Optically thick inner ejecta could prevent light from the rear side of the SN from penetrating, creating a flux deficit in the redshifted part of emission lines. The opacity could be caused by e.g. densely packed weak Fe transitions (electron-scattering turns out to be at least an order of magnitude too weak). To see the effect on the line profile, we created a simple model using a Monte Carlo code (see Fig. 5), where photons are absorbed or scattered on their way to an observer with a probability proportional to the ambient matter density (grey opacity). A profile calculated for an unrealistically early epoch of 30 d assuming pure elastic electron-scattering shows a characteristic tail on the red side, but too little blueshift of the line core to be consistent with observations at 100 d (see Fig. 5). This demonstrates that Thomson scattering provides too little opacity, and, furthermore, would modify the line profile in an undesired way if it were strong enough. If, instead, the calcu-

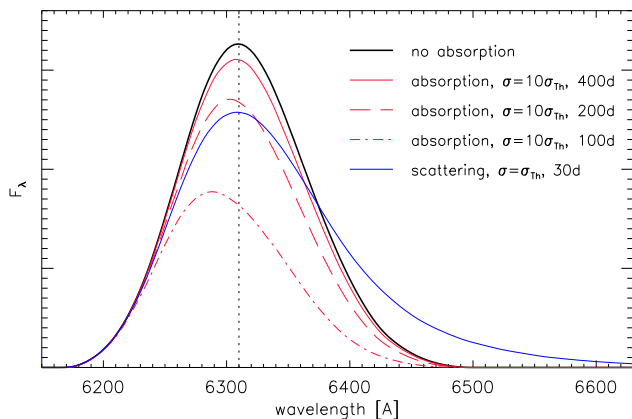


Figure 5. Synthetic profiles of [O I] $\lambda\lambda 6300, 6364$ calculated using a Monte Carlo code. A Gaussian density distribution, and both an emissivity and opacity proportional to the density have been assumed. The pure-scattering calculation is based on the Thomson cross-section σ_{Th} for e^- -scattering, assuming on average singly ionised material. The cases of pure absorption were computed using a grey opacity with $\sigma = 10\sigma_{\text{Th}}$. For comparison, the unabsorbed profile is also shown.

lations are performed for grey absorption, good results can be obtained if the cross section is chosen appropriately. In particular, the observed time evolution of the line blueshift is reproduced qualitatively thanks to the t^{-2} scaling of the column density.

5 STATISTICAL ANALYSIS, INFERRED EJECTA GEOMETRIES

The main intention of the multi-Gaussian line fitting is to derive information on the occurrence of different ejecta geometries in the sample. Of course, without additional assumptions it is not possible to restore the full 3D density distribution from its 1D projection given by the line profiles. While a forward calculation of emerging profiles for a given density distribution is straightforward, backward inference is highly degenerate.

A brief overview of some possible ejecta geometries and the corresponding observed line profiles is given in Table 3, illustrating that in several cases the geometry cannot be determined with confidence. Yet, for most observed profiles we can at least exclude certain configurations.

5.1 Taxonomy

Guided by the results of the multi-Gaussian fitting, we introduce four principal classes of line profiles. Note that this classification scheme is a simplistic choice, based on experience acquired during the fitting.

(i) *Gaussian profiles (GS)*, well reproduced by single-component fits, with the residuals showing no evidence of a second component within the noise level. These profiles are expected from spherically symmetric ejecta with a nearly Gaussian emissivity distribution, but could alternatively be the outcome of e.g. axisymmetric explosions viewed from intermediate angles ($40\text{--}50^\circ$, depending on the degree of asphericity; Maeda et al. 2008).

(ii) *Narrow-core lines (NC)*, characterised by an additional narrow component centred close to the rest wavelength and atop the broad base of the line (offsets $\lesssim 20 \text{ \AA}$). These are quite frequent and can be explained (a) by axisymmetric explosions with the emitting oxygen located in a torus or disk perpendicular to the line of sight (as inferred by Mazzali et al. 2001, Maeda et al. 2002 and Maeda et al. 2006 for SN 1998bw), (b) by spherically symmetric ejecta with an enhanced core density, or (c) by a blob of oxygen moving nearly perpendicularly to the line of sight [cf. (iv)]. Note that the presence of dense cores has been suggested for several SNe to explain their line profiles and late-time light-curve slopes (Iwamoto et al. 2000; Mazzali et al. 2000; Maeda et al. 2003; Mazzali et al. 2007a,b).

(iii) *Double-peaked profiles (DP)* with two comparably strong components, one blueshifted and the other redshifted by similar amounts. These are most readily explained by a torus-shaped oxygen distribution viewed nearly sideways (from angles of $\sim 60\text{--}90^\circ$ to the symmetry axis; Mazzali et al. 2005 and Maeda et al. 2008). No double peak can be realised in spherical symmetry. Hence, this class of line profile requires asphericity. The prototype of this class is SN 2003jd (Mazzali et al. 2005; Valenti et al. 2008).

(iv) *Multi-peaked or asymmetric profiles (AS)*, produced by additional components of arbitrary width and shift with respect to the main component. These profiles are either indicative of ejecta with large-scale clumping, a single massive blob, or a unipolar jet. Like the double peaks, they cannot be reproduced within spherical symmetry.

Assigning our sample of SNe to these categories is sometimes ambiguous. For instance, an [O I] feature which consists of a main peak and a Doppler-shifted blob may appear double-horned, and can be confused with genuine double peaks formed by a toroidal oxygen distribution as defined in (iii). A further complication for the classification arises from possible bulk shifts of the [O I] feature with respect to its rest wavelength: as discussed in Section 4 this does not necessarily have a geometric origin.

Fig. 6 indicates the class membership of individual SNe. Only SNe fitted with two components [classes (ii) to (iv)] are included in this figure, which shows the absolute wavelength offset between the two fit components (Table A1) as a function of α_w , the normalised flux of the weaker component. In this diagram, narrow-core SNe [class (ii)] populate a strip along the abscissa ($|\lambda_1 - \lambda_2| \lesssim 20 \text{ \AA}$), double peaks [class (iii)] an area of larger wavelength offset and $0.4 \lesssim \alpha_w \lesssim 0.5$, while SNe with asymmetric or multi-peaked profiles [class (iv)] are mostly contained in a region characterised by $\alpha_w \lesssim 0.3$ and $|\lambda_1 - \lambda_2| > 20 \text{ \AA}$. Note, however, that some objects lying in the narrow-core strip actually belong to class (iv), since their weaker component has too large an offset ($> 20 \text{ \AA}$) from the rest wavelength to fulfil the criteria defined for class (ii).

5.2 Statistical evaluation

In Table 4 the statistical summary of this analysis is presented. As we will see below, deviations from spherical symmetry affect all types of stripped-envelope CC-SNe, and are not reserved to particularly energetic or highly-stripped

Table 3. Selected oxygen geometries and corresponding line profiles.

Oxygen emissivity distribution	Line profile	Global symmetry
radial Gaussian	Gaussian	spherically symmetric
enhanced central density	narrow core on top	spherically symmetric
hard-edged homogeneous sphere	parabolic	spherically symmetric
spherical shell	flat-topped	spherically symmetric
torus viewed from top	narrow core	axisymmetric
torus viewed from the side	double peak, symmetric to λ_0	axisymmetric
torus viewed from intermediate angle	Gaussian-like	axisymmetric
small-scale clumpiness	fine-structured peak	asymmetric
unipolar jet, one-sided blob	extra-peaks / shoulders, shifted with respect to λ_0	asymmetric

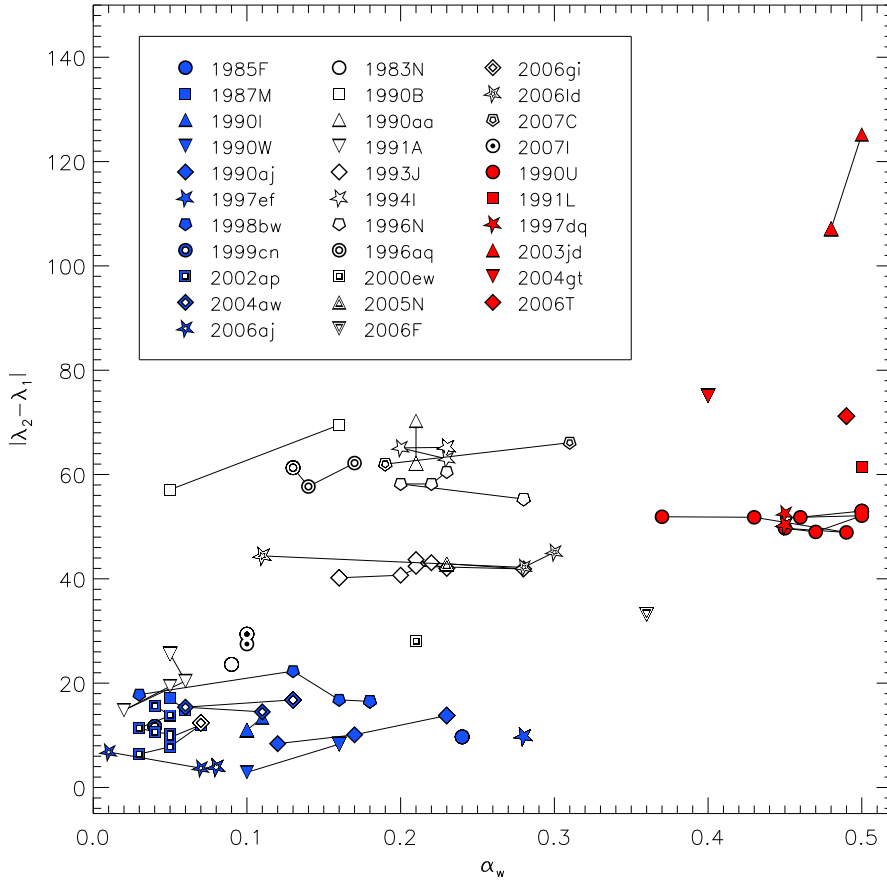


Figure 6. Absolute wavelength difference between two components found by multi-Gaussian fitting of [O I] $\lambda 6300$, as a function of α_w , the relative flux of the weaker component. Objects with single-Gaussian line profiles (cf. Fig. 2) are not shown. Filled blue symbols stand for narrow-core SNe, filled red symbols for double peaks, and open symbols for SNe with asymmetric or clumpy ejecta. The different classes appear fairly well separated in this plot.

events. This is in agreement with the results of Modjaz et al. (2008) and Maeda et al. (2008).

Spherically symmetric objects. SNe whose [O I] profiles are well fit with single Gaussians make up little more than a quarter of all objects, even within the uncertainties. Considering all possibly spherical SNe [i.e., classes (i) and (ii)], and again including objects with ambiguous classification, we

find their fraction to be just over 50%. Given that for some of these objects the S/N is too low to identify more than one component, that also jet-like explosions yield single-peaked symmetric profiles if viewed not too far from the jet axis, and that blobs moving roughly perpendicular to the line of sight can mimic narrow line cores, it is evident that this is really an upper limit for the number of spher-

Table 4. SN taxonomy in terms of [O I] line profiles. The errors account for possible alternative classifications as indicated in Fig. 2.

Category	Number	Percentage
(i) Gaussian	7^{+4}_{-2}	18^{+10}_{-5}
(ii) Narrow core	11^{+1}_{-4}	28^{+3}_{-10}
(iii) Double peak	6^{+1}_{-4}	15^{+3}_{-10}
(iv) Asymmetric / blobs	15^{+8}_{-4}	39^{+21}_{-10}

ical objects. This is exemplified by SN 1997X [class (i)], for which Wang et al. (2001) measured exceptionally strong continuum polarisation, of the order of 4%, clearly indicating globally aspherical ejecta. However, at the same time the [O I] profile reveals no obvious deviation from spherical symmetry (Fig. 2). Hence, SN 1997X is probably intrinsically aspherical, but viewed from a direction in which the line-of-sight projection of the oxygen emissivity mimics a spherical explosion. We thus speculate that probably more than half of all stripped-envelope CC-SNe are significantly aspherical.

Symmetric double peaks. Between 5 and 18% of the SNe in our sample belong to class (iii), i.e. their line profiles are best reproduced by a symmetric double-peak configuration. This suggests a somewhat lower occurrence rate of double peaks than the samples of Maeda et al. (2008) and Modjaz et al. (2008), where 28% and 37% of the SNe, respectively, were double-peaked. However, it should be noted that some of the double-peaked objects of Maeda et al. (2008) and Modjaz et al. (2008), such as SNe 2004ao, 2005aj and 2005bf, seem to lack symmetry about λ_0 , and might have been placed in class (iv) in our scheme.

Jet-SNe. In the jet-models of Maeda et al. (2006, 2008), oxygen is distributed in a torus-like geometry perpendicular to the jet axis, and the [O I] profile is strongly viewing-angle dependent (see Table 3). These models predict the ratio of narrow cores to double peaks to be $\sim 1:5$, rather insensitive to the degree of asphericity. On the contrary, we find fewer double-peaked profiles than narrow cores, suggesting that the majority of these narrow cores do not originate from jets, but e.g. from an enhanced central density. This also means that only a rather small fraction of all SNe Ib/c have a bipolar-jet geometry. In fact, depending on whether moderately (BP2 of Maeda et al. 2006) or strongly (BP8) aspherical models are used to evaluate the viewing-angle dependence of the profiles in detail, we find jet-SN fractions of $\sim 50\%$ or $\sim 25\%$ in our sample.

CC-SN subtypes. In Fig. 7 we show how the traditional stripped-envelope CC-SN subtypes (i.e., BL-Ic, Ic, Ib and IIb) are distributed in terms of line-profile classes. Although the total number of objects is too small for robust statements, we are tempted to attribute some significance to the trends we can discern. While SNe Ic, which form the majority of our sample (59%), are relatively homogeneously distributed, SNe Ib (21% of our sample) belong mainly to the multi-peaked / aspherical category. Finding objects with extended envelopes to show particularly strong asphericity appears counter-intuitive, and we have no convincing explanation for this behaviour. Similarly, broad-line SNe Ic (BL-Ic; $\sim 15\%$ of our sample) show a tendency towards nebular

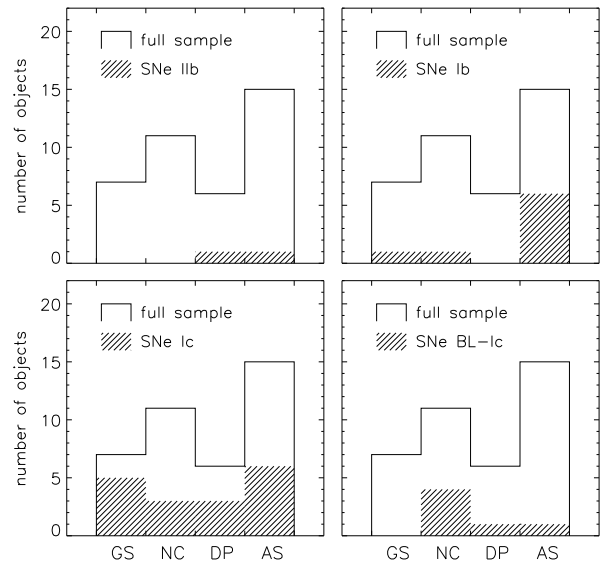


Figure 7. Allocation of the SNe in our sample to the line-profile classes defined in Section 5.1: GS stands for ‘Gaussian’ [class (i)], NC for ‘narrow core’ [class (ii)], DP for ‘double-peaked’ [class (iii)] and AS for ‘asymmetric / multi-peaked’ [class (iv)] (cf. Table 4). SNe IIb, SNe Ib, SNe Ic and BL-Ic SNe are separately shown in the different panels.

[O I] lines with narrow cores. At first, this seems to support the jet model. However, as discussed above, if all broad-line SNe Ic with narrow core were interpreted as jet-events, a much larger number of double peaks would be expected.² The FWHM of [O I] $\lambda 6300$ (taken from the one-component fits), averaged over all spectra, increases from SNe Ib/IIb ($5205 \pm 862 \text{ km s}^{-1}$) over normal-energetic SNe Ic ($5942 \pm 1376 \text{ km s}^{-1}$) to broad-line SNe Ic ($7343 \pm 1724 \text{ km s}^{-1}$), reflecting the trend found in early-time spectra. A similar result has already been reported by Matheson et al. (2001), whose data set is included here. However, also the variation of the FWHM from object to object increases in this direction, indicating particularly strong diversity in the ejecta geometry of BL-SNe Ic. An observed trend towards smaller FWHM at later epochs (see Fig. 8) could be explained by changes in the excitation conditions as a consequence of decreasing densities, such as a transition to more local positron deposition as the dominant excitation mechanism.

6 DISCUSSION OF INDIVIDUAL OBJECTS

In the previous sections we have presented simple Gaussian fits to the [O I] $\lambda \lambda 6300, 6364$ features in nebular spectra of 39 stripped-envelope CC-SNe, and found substantial diversity in the line profiles with deviations from spherical symmetry in a majority of the objects. However, remarkable patterns

² Note that the BL-Ic SNe 1998bw and 2006aj, members of the narrow-core class, were discovered only after the detection of their associated GRBs. Given the particular geometry imposed by a GRB connection, a mild bias may be introduced into our statistics. Since we assert no claim to a strictly unbiased sample, we included these two objects in our analysis throughout this work.

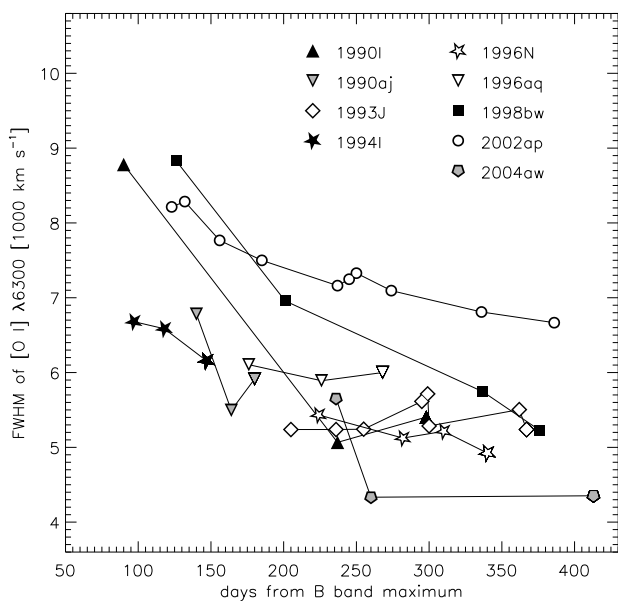


Figure 8. FWHM of the one-component Gaussian fit to the [O I] $\lambda 6300$ line as a function of time. Only selected SNe with good temporal coverage are displayed.

can also be discerned within the zoo of line profiles. In the following the properties of some interesting individual SNe or groups of objects are discussed in more detail.

6.1 SNe 1994I, 1996N and 1996aq: Doppler-shifted blobs and neutron-star kicks?

Sollerman et al. (1998) noticed a blueshift of [O I] $\lambda\lambda 6300, 6364$ in late-time spectra of SN 1996N. We confirm this result, obtaining an overall blueshift of 850 km s^{-1} in one-component fits. The epochs of the spectra are too late ($\geq 180 \text{ d}$) to explain this with optical-depth effects. In a two-component setup, which yields a much better fit to the asymmetric line profile, the main component is nearly at rest, but the second one is blueshifted by $\sim 3000 \text{ km s}^{-1}$ (Fig. 2 and Table A1), prominent and broad (FWHM = 2300 km s^{-1} , $\alpha \sim 0.2$ to 0.3).

Here we stress the similarity of the [O I] line profiles of SNe 1996N and 1994I (although the latter was only observed at earlier phases, not later than 150 d past maximum). Finding such an unusual [O I] profile in SN 1994I was unexpected, given that this is one of the most soundly studied SNe Ic to date, and, to our knowledge, this fact has never been commented on in the literature. SN 1996aq features an apparently different, double-peaked [O I] line. However, the fitting suggests that the main difference is the width of the blueshifted component, which is significantly narrower in SN 1996aq (FWHM = 1000 km s^{-1}). This results in a separation of the $\lambda 6300$ and $\lambda 6364$ lines and thus a two-horned appearance.

The most convincing explanation for the observed line profiles in these three SNe is provided by blobs moving towards the observer at high velocity. If such a blob has an average composition and no enhanced excitation (as would be the result of an enhanced Co abundance), it has to carry substantial mass to account for the observed emission. In

fact, in this simple scenario the mass fraction would be given by the fractional flux of the clump, α_w . In SN 1996aq, α_w is about 0.15, in SNe 1994I and 1996N 0.2–0.3. Moving at a velocity $\gtrsim 3000 \text{ km s}^{-1}$, the blob carries enormous momentum, which has to be counter-balanced for the sake of momentum conservation. Since the remainder of the oxygen emission is centred at rest, the compensation has to be provided by Fe- or Si-rich material, or the compact remnant of the core collapse. Strong neutron star kicks (up to several hundred km s^{-1}) have indeed been observed (e.g. Cordes, Romani & Lundgren 1993) and reproduced in simulations of anisotropic explosions with dominant dipole ($l = 1$) mode in the ejecta (Scheck et al. 2004, 2006). To estimate the kick velocities consistent with our measurements, we make a simple calculation for SN 1994I. With a total ejecta mass of $1.2 M_\odot$ (Sauer et al. 2006) and an α_w of 0.22, the blueshifted blob contains $0.26 M_\odot$ if a homogeneous composition is assumed throughout the ejecta. To compensate the momentum, a typical neutron star of $1.3 M_\odot$ needs a kick velocity of $\sim 600 \text{ km s}^{-1}$ if moving along the line of sight, which is not an unreasonable number.

6.2 SNe 1998bw and 2002ap: narrow cores?

SNe 1998bw and 2002ap share a similar [O I] $\lambda\lambda 6300, 6364$ line profile with a narrow component on top of a much broader base. In SN 1998bw, this was attributed to emission from a disk- or torus-shaped oxygen distribution viewed nearly from the top (Mazzali et al. 2001; Maeda et al. 2002, 2006). Together with Fe lines being broader than [O I] $\lambda\lambda 6300, 6364$, this gave rise to the idea of a strongly aspherical, jet-like explosion. For the nebular spectra of SN 2002ap, Foley et al. (2003) remarked on a similarity of the line profiles with those of SN 1998bw, and Mazzali et al. (2007a) suggested asphericity here as well, although the narrow peak might have been caused by a dense core in the ejecta.

However, in both SNe the narrow components are redshifted with respect to both the broad base and the rest wavelength λ_0 (Patat et al. 2001; Leonard et al. 2002; Foley et al. 2003). From the best-fit parameters reported in Table A1, mean redshifts of $586 \pm 162 \text{ km s}^{-1}$ and $657 \pm 62 \text{ km s}^{-1}$ with respect to λ_0 are inferred for SNe 1998bw and 2002ap, respectively (cf. Fig 9). Relative to the broad bases, mean offsets of $876 \pm 129 \text{ km s}^{-1}$ and $500 \pm 138 \text{ km s}^{-1}$ are observed. Such large offsets (comparable to the narrow component's FWHM) are not expected for models with enhanced central density or the bipolar-jet scenario favoured for SN 1998bw. Instead, the nebular [O I] lines should be symmetric and centred at their rest wavelength unless the putative jet was rather one-sided. In that case, the lack of symmetry between the two hemispheres would explain the observed [O I] line shifts. In this work, we conservatively classify SNe 1998bw and 2002ap as *possible* narrow cores (Fig. 2), considering the presence of a blob another possibility. Other SNe of the narrow-core group exhibit similar line offsets (cf. Table A1), but mostly less pronounced than in SNe 1998bw and 2002ap.

Inspired by the modelling of Tomita et al. (2006) and Mazzali et al. (2007a), we examined an alternative, possibly more physical configuration for SN 2002ap. This consisted of a jet (or, more generically, a bipolar explosion) viewed strongly off-axis, but with an additional density enhance-

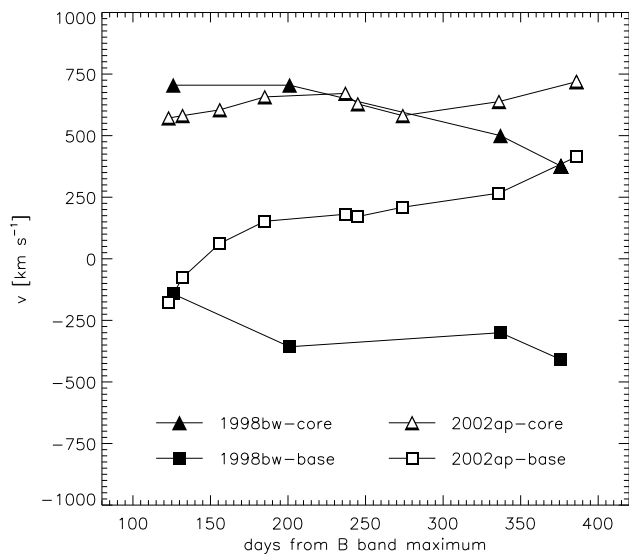


Figure 9. Shifts of the broad line bases and the narrow cores of [O I] $\lambda 6300$ in SNe 1998bw and 2002ap as a function of time (cf. Table A1).

ment at low velocity. To test the consistency with the observed [O I] line profile, we employed a three-component fit consisting of a strictly symmetric double peak plus a central narrow component (7 effective parameters; see Table A2), and compared with the ‘broad peak + narrow core’ setup adopted for SN 2002ap throughout the rest of this paper.

It turns out that the two configurations perform similarly well, the only advantage of the two-component fit being that one fewer parameter is involved. It is therefore difficult to decide on the basis of these fits which ejecta geometry (on-axis jet, spherical ejecta + dense core, spherical ejecta + blob or off-axis jet + dense core) is most likely. In the ‘DP + NC’ configuration, about 15% of the emitting mass would be contained in the dense core. This is in good agreement with the size of the core that was added to reproduce the late-time light curve of SN 2002ap in the models (0.5 out of a total of $3.0 M_{\odot}$; Tomita et al. 2006). The good quality of the fit and the consistency with sophisticated modelling make the ‘DP + NC’ scenario an attractive possibility for SN 2002ap.³

6.3 SNe 2003jd, 2000ew, 2004gt and 2006T: genuine double peaks and impostors

Besides SNe 2003jd and 2006T, the prototypes of the double-peaked class, up to 5 other SNe have [O I] lines that agree with a DP configuration. The problem with most of these objects is that the separation of the two fit components is

³ Also other SNe of the narrow-core class can be adequately fit with three components in a configuration similar as in SN 2002ap. This could help to solve the ‘problem of missing double peaks’, see Section 5.2). However, for the GRB-related SNe 1998bw and 2006aj a ‘DP + NC’ configuration – though providing a good fit (cf. Table A2) – is not expected to be correct, since these SNe are supposed to be viewed along the jet axis. Lacking modelling predictions for most other SNe, we have not explored the ‘DP + NC’ option any further.

smaller than in SNe 2003jd and 2006T, and often similar to the separation of the two [O I] lines in the doublet. This leaves room for alternative interpretations, in particular the possibility that the two horns observed e.g. in SNe 2000ew and 2004gt may actually originate from the deblended $\lambda 6300$ and $\lambda 6364$ lines of a single narrow, blueshifted component. In fact, in SN 2000ew the line profile is better reproduced by the latter configuration. This is the reason for its primary association with the AS class (see Fig. 2).

In SNe 2000ew and 2004gt also the intensity ratio of the two peaks appears inverted with respect to those of SNe 2003jd and 2006T, the blue peak being stronger than the red one. In a classical DP configuration (cf. Section 5.1), however, the red peak will always be stronger since, for the given separation of the peaks, the $\lambda 6364$ -line of the blue component blends with the $\lambda 6300$ -line of the red one. To circumvent this problem, a more complex ejecta structure with additional blueshifted emission on top of an otherwise symmetric profile may be assumed. This yields a good fit for SN 2004gt, cf. Table A2. Alternatively, the original toroidal oxygen distribution may be unchanged, but the redshifted emission component is damped owing to optically thick inner ejecta (cf. Section 4). Since the spectra of SNe 2000ew and 2004gt are both relatively young (112 and 160 d, respectively) compared to those of SNe 2003jd and 2006T (cf. Table 1), this may indeed be a possibility.

Due to its ejecta velocities and its double-peaked [O I] profile, SN 2003jd has been proposed to be associated with a GRB viewed strongly off-axis (Mazzali et al. 2005). In that case, the γ - and X-ray emission of the GRB would not be seen because of the strong collimation of the jet. However, depending on the jet propagation model a radio afterglow would possibly be observable at late phases. SN 2003jd was not detected at radio wavelengths (Soderberg et al. 2006), so that its association with a GRB remains uncertain. The second object with a similar [O I] line profile, SN 2006T, was classified as SN Iib (Blondin et al. 2006). This makes it *per se* a poor candidate for a GRB-SN, since the relativistic jet of a GRB would have to penetrate the He and H shells and probably die before reaching the surface. This supports the view of Modjaz et al. (2008) and Maeda et al. (2008) that strong asphericity is ubiquitous in core-collapse SNe, and not necessarily a signature of an association with a GRB (see also Section 5.2).

7 THE PROFILE OF Mg I] $\lambda 4571$

Hydrodynamic explosion models (Maeda et al. 2006) suggest that Mg and O should have similar spatial distributions within the SN ejecta, which may deviate significantly from those of heavier elements such as Fe or Ca (see also Mazzali et al. 2005). This should result in the profiles of isolated Mg and O emission lines being similar, which so far has been shown to hold for individual SNe (Spyromilio 1994; Foley et al. 2003). Here we test this for our entire sample, examining the profile of the semi-forbidden Mg I] $\lambda 4571$ line ($3s^2 \ ^1S_0 - 3s3p \ ^3P^{\circ}_1$) in all spectra with sufficient S/N in the wavelength range of interest.

A direct comparison of the Mg I] and [O I] lines is hindered by the fact that, unlike Mg I], the [O I] feature is a doublet. However, as described in Section 3.2, we assumed

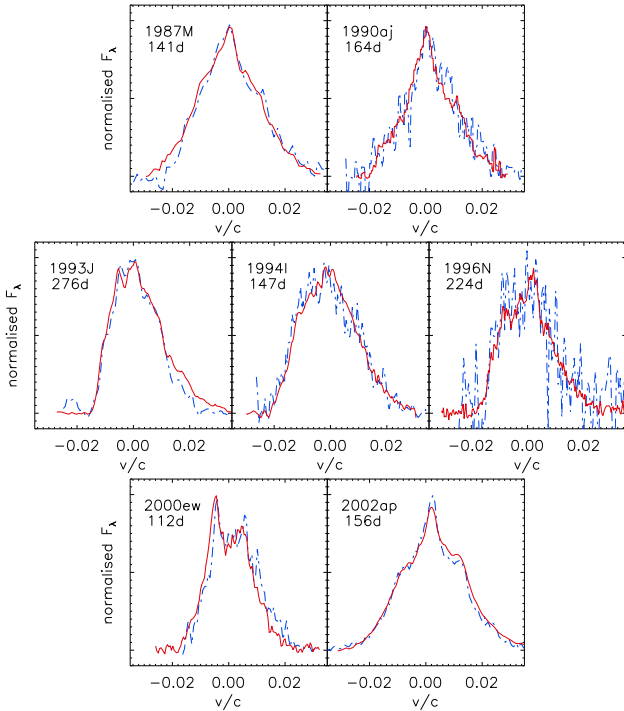


Figure 10. Comparison of Mg I $\lambda 4571$ and [O I] $\lambda\lambda 6300, 6364$ line profiles (with a second component added to Mg I artificially to account for the doublet nature of [O I], see discussion). A sub-sample of objects with a good overlap is shown. The dot-dashed blue line is the modified Mg I, the solid red line [O I].

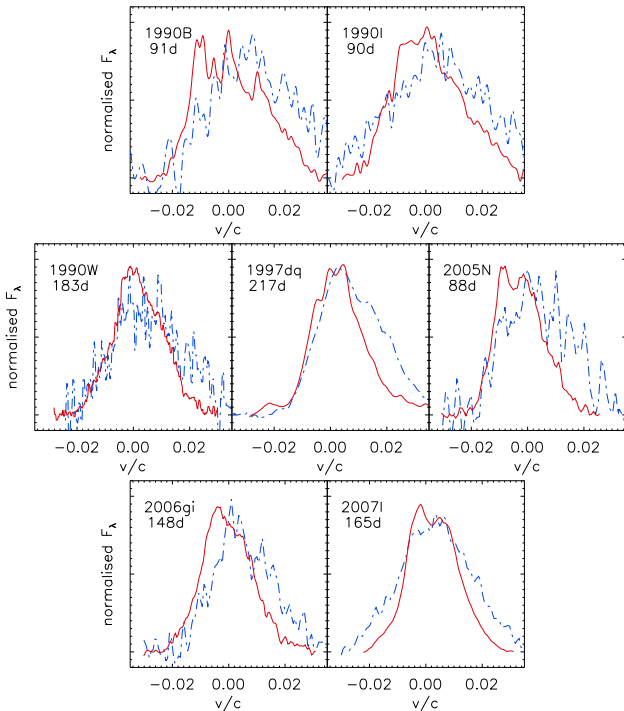


Figure 11. The same as Fig. 10, but showing spectra with evident differences in the [O I] $\lambda\lambda 6300, 6364$ and the modified Mg I $\lambda 4571$ profiles.

that in our nebular SN Ib/c spectra the $\lambda 6300$ and $\lambda 6364$ lines have a ratio of 3 : 1. Therefore, to compensate we first isolated the Mg I $\lambda 4571$ feature, subtracting a linearly fit background. Then we rescaled the Mg I line to 1/3 of its initial intensity, shifted it by 46 \AA (equivalent to the 64 \AA offset of the two [O I] lines) and added it to the original profile. This modified Mg I profile can then be compared with the observed [O I] feature.

For most objects of our sample ($\sim 65\%$), even those with rather complex ejecta geometry, we find an impressive similarity of the Mg I and [O I] line profiles within the noise level and the uncertainty in subtracting the background (see Fig. 10). This indicates that the spatial distribution of Mg and O in the ejecta is generally similar. However, there are some noticeable exceptions with a poor match of the [O I] and modified Mg I features. Examples are shown in Fig. 11. Most of these spectra are not very late, typically < 200 d, which leaves room for the following explanations:

(i) In the affected objects, the O- and Mg-rich parts of the ejecta may indeed have different geometry owing to the chemical stratification of the progenitor star and the hydrodynamics of the explosion. However, within this scenario differences in the line profiles should persist during the entire nebular phase. In SN 1998bw, for which a late nebular spectrum (376 d) is available, the differences visible at earlier epochs ($\lesssim 200$ d) are observed to vanish with time (Fig. 12). SN 2007C undergoes a similar evolution even more rapidly.

(ii) Alternatively, the Mg I or the [O I] features may be contaminated by nebular emission lines of other elements. For the [O I] feature the possibility of a contamination on the blue side has been discussed in Section 4, and found to be unlikely. Also, the fact that in most of the affected spectra the Mg I line is broader than the [O I] line and changes more strongly with time (cf. Figs. 11 and 12) suggests that the Mg I rather than the [O I] line may be blended with other lines at early epochs.

(iii) The Mg I $\lambda 4571$ line is located in a region shaped by many strong Fe II features during the photospheric phase. Hence, it is possible that the emission peak tentatively identified as Mg I is mostly produced by underlying photospheric Fe lines in some earlier spectra. This would not only explain the observed evolution in SN 1998bw (where Fe features are particularly strong and persistent, see e.g. Mazzali et al. 2005), but also the better agreement of [O I] and Mg I in SN 2002ap early on: SN 2002ap features the strongest Mg I $\lambda 4571$ line ever observed (Foley et al. 2003) but only weak Fe, and it is hence not unexpected that Mg I quickly dominates over photospheric residuals (Fig. 12).

8 CONCLUSIONS

We have studied the profiles of nebular emission lines in stripped-envelope CC-SNe, with the aim of constraining the ejecta morphology, and in particular the degree of asphericity of the explosions. The study was based on 98 nebular spectra of 39 different SNe, some of which were not published before. The size of the sample gives it statistical significance. We have concentrated on the profile of [O I] $\lambda\lambda 6300, 6364$, since this is usually the strongest feature in nebular SN Ib/c spectra, and not severely contaminated by other lines. We performed a multi-parameter Gauss-fitting of this feature in

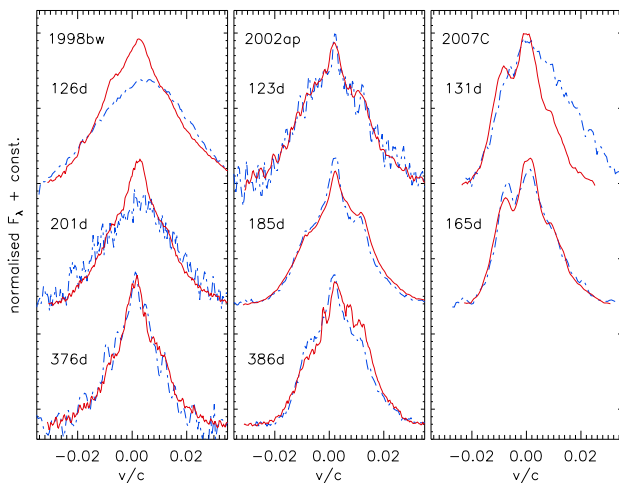


Figure 12. Evolution of the [O I] $\lambda\lambda 6300, 6364$ (solid red) and the modified Mg I] $\lambda 4571$ (dot-dashed blue) line profiles of SNe 1998bw, 2002ap and 2007C with phase. While in SN 2002ap the profiles are always similar, significant differences are apparent in the earlier spectra of SNe 1998bw and 2007C.

all our spectra, with the position, FWHM and intensity of the $\lambda 6300$ Gaussian being free parameters (and the $\lambda 6364$ line duly added with fixed offset and intensity ratio of 1/3). Using this approach, a variable number of emission components, their widths and Doppler shifts could be identified. Compared to spectral modelling this method has the advantage of being fast, capable of dealing with complex profiles, and independent of an accurate flux calibration.

Despite the large variety in line profiles encountered, we can divide the SNe into four morphologically different groups on the basis of the best-fit parameters: SNe with simple Gaussian line profiles ($\sim 18\%$ of all objects), SNe with narrow line cores atop broad bases ($\sim 28\%$), objects with symmetric double peaks ($\sim 15\%$), and objects with evidence for blobs or overall asymmetric line profiles ($\sim 39\%$). Since this classification refers to the structure inferred from the fitting procedure, we believe it to be more relevant for the true ejecta geometry than a pure visual inspection of the line. The results of our analysis suggest that probably at least half of all SNe Ib/c are aspherical. The fraction of double peaks is too small for a jet to be a ubiquitous feature in a majority of the objects. Even among narrow-core SNe, only a small fraction of the objects may have a jet-like ejecta morphology. Instead, a central density enhancement appears to be a likely solution for many members of this class. A majority of broad-line SNe Ic have narrow line cores, whereas most SNe Ib exhibit asymmetric or multi-peaked line profiles.

Bulk shifts of the [O I] feature and strongly Doppler-shifted, massive blobs are observed in some objects, and expected to be the signature of very one-sided explosions. If momentum conservation is provided by neutron-star kicks, the inferred kick velocities are compatible with those of the fastest-moving neutron-stars in the Galaxy.

In spectra taken earlier than ~ 200 d after maximum light, a systematic blueshift of the [O I] $\lambda\lambda 6300, 6364$ line centroids can be discerned, becoming more pronounced with decreasing phase. Geometrical effects and dust formation

within the ejecta seem to be excluded as origins of the blueshift. Contamination from other elements may play a role in some, but not all SNe. Hence, residual opacity in the inner ejecta remains the most likely explanation for the observed shift, as photons emitted on the rear side of the SN are scattered or absorbed on their way through the ejecta, giving rise to a flux deficit in the redshifted part of spectral emission lines. The required opacity might be generated by a multitude of weak Fe transitions.

A surprisingly good agreement of the profiles of [O I] $\lambda\lambda 6300, 6364$ and Mg I] $\lambda 4571$ (modified to account for the doublet nature of the oxygen feature) was found in most SNe regardless of their morphological class. This indicates that the line profiles are indeed determined by the ejecta geometry, and that Mg and O are similarly distributed within the SN ejecta. Deviations are mainly found in relatively early spectra, and we propose blending of the emerging nebular Mg I] emission with residual photospheric Fe II lines as a possible reason for the differences.

ACKNOWLEDGMENTS

ST is grateful to Marilena Salvo for kindly agreeing to the use of a previously unpublished spectrum of SN 2002ap obtained at Siding Spring Observatory. He also wants to thank Bruno Leibundgut, Daniel Sauer, Luca Zampieri and Maryam Modjaz for stimulating discussions and helpful comments. SB, EC and MT are supported by the Italian Ministry of Education via the PRIN 2006 n.2006022731 002 and ASI/INAF grant n. I/088/06/0. KM acknowledges the support by World Premier International Research Center Initiative, MEXT.

This work is based on data collected with the 3.6 m, 2.2 m, 1.5 m and Danish Telescopes at ESO–La Silla (programme numbers 145.4-0004, 057.D-0534, 058.D-0307, 059.D-0332, 060.D-0415, 061.D-0630, 065.H-0292 and 066.D-0683), the 8.2 m VLT-U1 at ESO–Paranal (programme numbers 075.D-0662, 078.D-0246 and 079.D-0716), the 2.3 m Telescope at Siding Spring Observatory and the 2.56 m Nordic Optical Telescope at Roque de los Muchachos Observatory.

The authors made use of the Asiago Supernova Catalogue, the NASA/IPAC Extragalactic Database (NED) which is operated by the Jet Propulsion Laboratory, California Institute of Technology, under contract with the National Aeronautics and Space Administration; the Lyon-Meudon Extragalactic Database (LEDA), supplied by the LEDA team at the Centre de Recherche Astronomique de Lyon, Observatoire de Lyon; the NIST Atomic Spectra Database, provided by the National Institute of Standards and Technology, Gaithersburg; the Online Supernova Spectrum Archive (SUSPECT), initiated and maintained at the Homer L. Dodge Department of Physics and Astronomy, University of Oklahoma; and the Bright Supernova web pages, maintained by David Bishop as part of the International Supernovae Network (<http://www.supernovae.net>).

REFERENCES

- Barbon R., Benetti S., Cappellaro E., Patat F., Turatto M., 1993, *MmSAI*, 64, 1083
- Barbon R., Benetti S., Cappellaro E., Patat F., Turatto M., Iijima T., 1995, *A&AS*, 110, 513
- Blondin J. M., Mezzacappa A., DeMarino C., 2003, *ApJ*, 584, 971
- Blondin S., Modjaz M., Kirshner R., Challis P., Matheson T., 2006, *CBET* 386
- Chugai N. N., 1992, *SvAL*, 18, 239
- Clocchiatti A., et al., 2001, *ApJ*, 553, 886
- Cordes J. M., Romani R. W., Lundgren S. C., 1993, *Nature*, 362, 133
- Danziger I. J., Gouiffes C., Bouchet P., Lucy L. B., 1989, *IAUC* 4746, 1
- Elmhamdi A., et al., 2003, *MNRAS*, 338, 939
- Elmhamdi A., Danziger I. J., Cappellaro E., Della Valle M., Gouiffes C., Phillips M. M., Turatto M., 2004, *A&A*, 426, 963
- Ferrero P., et al., 2006, *A&A*, 457, 857
- Filippenko A. V., Sargent W. L. W., 1986, *AJ*, 91, 691
- Filippenko A. V., Sargent W. L. W., 1989, *ApJ*, 345, L43
- Filippenko A. V., Porter A. C., Sargent W. L. W., 1990, *AJ*, 100, 1575
- Filippenko A. V., et al., 1995, *ApJ*, 450, L11
- Foley R. J., et al., 2003, *PASP*, 115, 1220
- Fransson C., Chevalier R. A., 1987, *ApJ*, 322, L15
- Fransson C., Chevalier R. A., 1989, *ApJ*, 343, 323
- Galama T. J., et al., 1998, *Nature*, 395, 670
- Gaskell C. M., Cappellaro E., Dinerstein H. L., Garnett D. R., Harkness R. P., Wheeler J. C., 1986, *ApJ*, 306, L77
- Gómez G., López R., 1994, *AJ*, 108, 195
- Gómez G., López R., 2002, *AJ*, 123, 328
- Guetta D., Della Valle M., 2007, *ApJ*, 657, L73
- Harutyunyan A., et al., 2008, *A&A*, 488, 383
- Horne K., 1986, *PASP*, 98, 609
- Iwamoto K., et al., 2000, *ApJ*, 534, 660
- Kifonidis K., Plewa T., Scheck L., Janka H.-T., Müller E., 2006, *A&A*, 453, 661
- Leibundgut B., Kirshner R. P., Pinto P. A., Rupen M. P., Smith R. C., Gunn J. E., Schneider D. P., 1991, *ApJ*, 372, 531
- Leonard D. C., Filippenko A. V., Chornock R., Foley R. J., 2002, *PASP*, 114, 1333
- Li H., McCray R., 1992, *ApJ*, 387, L309
- Lucy L. B., Danziger I. J., Gouiffes G., Bouchet P., 1989, in Tenorio-Tagle G., Moles M., Melnick J., eds, *Proceedings of IAU Colloquium 120 "Structure and Dynamics of the Interstellar Medium"*. Springer, Berlin, p. 164
- Maeda K., Nakamura T., Nomoto K., Mazzali P. A., Patat F., Hachisu I., 2002, *ApJ*, 565, 405
- Maeda K., Mazzali P. A., Deng J., Nomoto K., Yoshii Y., Tomita H., Kobayashi Y., 2003, *ApJ*, 593, 931
- Maeda K., Nomoto K., Mazzali P. A., Deng J., 2006, *ApJ*, 640, 854
- Maeda K., et al., 2008, *Sci*, 319, 1220
- Matheson T., Filippenko A. V., Ho L. C., Barth A. J., Leonard D. C., 2000, *AJ*, 120, 1499
- Matheson T., Filippenko A. V., Li W. D., Leonard D. C., Shields J. C., 2001, *AJ*, 121, 1648
- Matthews K., Neugebauer G., Armus L., Soifer B. T., 2002, *AJ*, 123, 753
- Mazzali P. A., Iwamoto K., Nomoto K., 2000, *ApJ*, 545, 407
- Mazzali P. A., Nomoto K., Patat F., Maeda K., 2001, *ApJ*, 559, 1047
- Mazzali P. A., et al., 2005, *Sci*, 308, 1284
- Mazzali P. A., et al., 2007a, *ApJ*, 661, 892
- Mazzali P. A., et al., 2007b, *ApJ*, 670, 592
- Modjaz M., Kirshner R. P., Challis P., 2008, *ApJ*, 687, L9
- Patat F., Chugai N., Mazzali P. A., 1995, *A&A*, 299, 715
- Patat F., et al., 2001, *ApJ*, 555, 900
- Phillips M. M., Williams R. E., 1991, in Woosley S. E., ed, *Proceedings to the Tenth Santa Cruz Workshop in Astronomy and Astrophysics "Supernovae"*. Springer, New York, p. 36
- Podsiadlowski Ph., Mazzali P. A., Nomoto K., Lazzati D., Cappellaro E., 2004, *ApJ*, 607, L17
- Sauer D., Mazzali P. A., Deng J., Valenti S., Nomoto K., Filippenko A. V., 2006, *MNRAS*, 369, 1939
- Scheck L., Plewa T., Janka H.-T., Kifonidis K., Müller E., 2004, *PhRvL*, 92, 011103
- Scheck L., Kifonidis K., Janka H.-T., Müller E., 2006, *A&A*, 457, 963
- Soderberg A. M., Nakar E., Berger E., Kulkarni S. R., 2006, *ApJ*, 638, 930
- Sollerman J., Leibundgut B., Spyromilio J., 1998, *A&A*, 337, 207
- Spyromilio J., 1991, *MNRAS*, 253, 25
- Spyromilio J., 1994, *MNRAS*, 266, L61
- Spyromilio J., Pinto P. A., 1991, in Danziger I. J., Kjær K., eds, *Proceedings to the ESO/EIPC Workshop "Supernova 1987A and other supernovae"*. ESO, Garching, p. 423
- Taubenberger S. et al., 2006, *MNRAS*, 371, 1459
- Tomita H., et al., 2006, *ApJ*, 644, 400
- Tsvetkov D. Y., 1986, *SvAL*, 12, 328
- Turatto M., 2000, *MmSAI*, 71, 573
- Turatto M., 2003, in "Supernovae and Gamma-Ray Bursters", Weiler K. W., ed, series: *Lecture Notes in Physics*, vol. 598, Springer, Berlin, p. 21
- Valenti S., et al., 2008, *MNRAS*, 383, 1485
- Wang L., Hu J., 1994, *Nature*, 369, 380
- Wang L., Howell D. A., Höflich P., Wheeler J. C., 2001, *ApJ*, 550, 1030

APPENDIX A: FIT PARAMETERS

In the following tables the parameters of the best fits to the [O I] features of our spectra are reported. All numbers refer to the $\lambda 6300$ line, since the $\lambda 6364$ line is automatically added by the fitting algorithm at 1/3 of the strength. One- and two-component fits have been obtained for all SNe. They are listed in Table A1, along with error estimates for the one-component fit parameters. Three-component fits have only been performed for a few objects. In SNe 1990B, 2006ld and 2007C the line profiles were too complex to be satisfactorily reproduced with fewer components, while for SNe 1997dq, 1998bw, 2002ap and 2006aj particular ejecta geometries were tested. The three-component fit parameters are reported in Table A2.

Table A1. Parameters^a of the best one-component (cols. 4–5) and two-component (cols. 6–12) fits of [O I] λ 6300 – 1^{at} part.

SN (1)	Date (2)	Sample region (3)	λ (4)	FWHM (5)	λ_1 (6)	FWHM ₁ (7)	α_1 (8)	λ_2 (9)	FWHM ₂ (10)	α_2 (11)	rel. RMS ^b (12)
1983N	1983/03/01	6195.9–6455.8	6300.8 ± 2.7	97.1 ± 1.5	6297.3	100.6	0.91	6320.9	46.0	0.09	0.545
1985F	1985/03/19	6165.0–6477.0	6294.7 ± 1.7	87.1 ± 3.0	6290.7	112.0	0.76	6300.4	40.4	0.24	0.062
1987M	1988/02/09	6125.9–6530.6	6284.9 ± 3.1	151.8 ± 3.0	6283.3	158.8	0.95	6300.4	31.6	0.05	0.494
	1988/02/25	6114.3–6495.3	6284.5 ± 4.4	141.0 ± 9.0	6282.8	149.4	0.94	6297.6	37.6	0.06	0.774
1988L	1988/07/17	6114.2–6491.7	6266.3 ± 6.4	157.7 ± 13.0	-	-	-	-	-	-	-
	1988/09/15	6147.8–6467.0	6285.7 ± 10.3	147.1 ± 30.0	-	-	-	-	-	-	-
1990B	1990/04/18	6132.1–6499.7	6285.5 ± 3.5	183.2 ± 3.0	6305.1	185.8	0.84	6235.6	36.6	0.16	0.230
	1990/04/30	6192.4–6499.6	6292.5 ± 6.0	194.5 ± 12.0	6299.4	198.7	0.95	6242.3	16.7	0.05	0.688
1990I	1990/07/26	6114.5–6563.7	6287.3 ± 2.5	184.4 ± 3.0	6309.4	192.1	0.76	6250.8	86.3	0.24	0.345
	1990/12/21	6171.2–6458.0	6300.2 ± 2.5	106.4 ± 2.0	6297.1	119.0	0.89	6310.5	30.0	0.11	0.454
	1991/02/20	6178.6–6466.8	6298.5 ± 6.4	113.5 ± 15.0	6296.1	125.4	0.90	6307.1	24.9	0.10	0.837
1990U	1990/10/20	6189.8–6443.9	6283.5 ± 4.1	91.3 ± 6.0	6267.3	63.7	0.63	6319.2	73.1	0.37	0.578
	1990/10/24	6197.7–6435.5	6287.0 ± 4.1	88.2 ± 3.6	6268.0	54.1	0.57	6319.8	65.8	0.43	0.349
	1990/11/23	6183.1–6463.6	6292.6 ± 3.7	89.6 ± 2.0	6270.9	49.6	0.49	6319.8	68.8	0.51	0.213
	1990/11/28	6203.2–6457.3	6295.3 ± 5.3	89.7 ± 9.0	6270.0	47.9	0.45	6319.7	69.1	0.55	0.373
	1990/12/12	6195.7–6451.1	6291.5 ± 5.3	96.4 ± 6.0	6268.6	54.3	0.47	6317.6	77.5	0.53	0.619
	1990/12/20	6215.4–6448.5	6292.2 ± 3.8	92.8 ± 2.0	6269.0	48.8	0.50	6321.1	66.4	0.50	0.255
	1991/01/06	6193.9–6443.0	6294.6 ± 3.8	93.3 ± 5.0	6270.5	48.9	0.46	6322.3	71.6	0.54	0.268
	1991/01/12	6198.4–6465.8	6293.1 ± 3.9	93.9 ± 4.0	6270.3	52.4	0.50	6323.3	73.9	0.50	0.309
1990W	1991/02/21	6168.0–6449.5	6295.1 ± 3.0	106.9 ± 3.0	6295.6	120.2	0.90	6292.7	40.6	0.10	0.499
	1991/04/21	6144.0–6496.8	6295.5 ± 3.0	107.9 ± 1.0	6298.0	125.1	0.84	6289.7	46.5	0.16	0.290
1990aa	1991/01/12	6128.2–6516.7	6283.3 ± 3.8	184.4 ± 8.8	6306.8	191.0	0.79	6236.5	77.5	0.21	0.618
	1991/01/23	6128.5–6504.9	6283.3 ± 4.3	165.8 ± 13.0	6300.5	164.7	0.79	6238.4	96.2	0.21	0.912
1990aj	1991/01/29	6150.1–6498.6	6294.1 ± 2.0	142.4 ± 3.0	6292.2	162.7	0.88	6300.6	46.2	0.12	0.491
	1991/02/22	6170.4–6450.2	6292.9 ± 2.0	115.4 ± 5.0	6289.7	141.1	0.83	6299.8	40.6	0.17	0.287
	1991/03/10	6149.3–6492.6	6296.6 ± 8.2	124.2 ± 19.0	6290.8	158.6	0.77	6304.6	44.3	0.23	0.706
1991A	1991/03/22	6134.9–6467.6	6264.1 ± 3.5	112.5 ± 5.5	6266.0	116.2	0.95	6246.6	34.5	0.05	0.671
	1991/04/07	6137.7–6469.1	6276.1 ± 5.4	124.4 ± 11.0	6276.8	127.7	0.98	6262.0	18.9	0.02	0.899
	1991/04/16	6135.6–6480.0	6276.4 ± 2.2	120.8 ± 3.0	6278.5	125.3	0.94	6258.1	39.8	0.06	0.647
	1991/06/08	6137.1–6508.2	6286.5 ± 2.0	126.1 ± 3.0	6289.1	130.4	0.95	6263.5	31.7	0.05	0.340
1991L	1991/06/08	6156.3–6444.7	6289.5 ± 5.5	105.2 ± 6.5	6258.9	65.5	0.50	6320.4	67.6	0.50	0.694
1991N	1991/12/14	6191.9–6457.6	6303.9 ± 3.6	106.1 ± 8.0	6303.7	106.1	0.77	6304.3	105.9	0.23	1.048
	1992/01/09	6191.0–6472.7	6303.5 ± 2.8	104.0 ± 5.0	6304.5	123.9	0.68	6302.8	74.9	0.32	0.943
1993J ^c	1993/10/19	6172.2–6512.2	6279.7 ± 4.2	110.0 ± 2.0	6307.1	115.7	0.55	6257.6	73.4	0.45	0.525
	1993/11/19	6192.2–6512.2	6294.3 ± 4.3	110.0 ± 2.0	6307.3	114.4	0.77	6265.3	54.2	0.23	0.404
	1993/12/08	6195.7–6512.2	6295.8 ± 4.2	110.1 ± 2.0	6308.4	109.2	0.79	6264.7	54.4	0.21	0.460
	1994/01/17	6176.4–6512.0	6292.6 ± 4.2	117.9 ± 2.0	6304.2	110.1	0.79	6261.8	54.2	0.21	0.500
	1994/01/21	6188.6–6513.1	6289.2 ± 4.2	120.0 ± 1.5	6303.8	114.7	0.72	6261.9	63.4	0.28	0.421
	1994/01/22	6178.6–6514.3	6293.4 ± 4.7	111.0 ± 4.0	6305.2	110.0	0.78	6262.1	54.3	0.22	0.469
	1994/03/25	6183.9–6514.1	6295.9 ± 4.6	115.6 ± 4.0	6306.4	108.9	0.80	6265.7	57.1	0.20	0.574
	1994/03/30	6191.3–6518.9	6302.3 ± 4.6	110.0 ± 6.0	6309.7	104.0	0.84	6269.5	50.5	0.16	0.635
1994I	1994/07/14	6130.9–6497.4	6275.6 ± 2.0	140.3 ± 2.0	6294.6	129.2	0.77	6231.6	62.4	0.23	0.169
	1994/08/04	6140.0–6493.2	6279.9 ± 2.7	138.3 ± 2.0	6296.3	127.5	0.80	6231.2	62.0	0.20	0.209
	1994/09/02	6160.3–6469.5	6277.4 ± 2.7	129.3 ± 4.0	6294.9	111.3	0.77	6229.7	60.0	0.23	0.289
1995bb	1995/12/17	6157.7–6470.4	6296.6 ± 6.9	145.0 ± 12.0	6292.3	152.3	0.93	6321.8	45.6	0.07	0.929
1996D	1996/09/10	6150.8–6483.0	6301.3 ± 7.9	152.2 ± 15.0	6288.6	158.0	0.87	6337.4	39.6	0.13	0.767
1996N	1996/10/19	6164.7–6471.2	6283.7 ± 5.0	114.1 ± 5.0	6299.5	94.4	0.77	6239.0	46.1	0.23	0.414
	1996/12/16	6177.7–6465.1	6281.1 ± 5.0	107.6 ± 5.0	6295.6	89.6	0.78	6237.4	47.0	0.22	0.449
	1997/01/13	6174.5–6458.2	6282.2 ± 5.0	109.5 ± 5.0	6294.9	94.9	0.80	6236.7	51.2	0.20	0.754
	1997/02/12	6173.0–6453.2	6282.6 ± 5.0	103.4 ± 5.0	6300.4	81.8	0.72	6245.1	45.8	0.28	0.389
1996aq	1997/02/11	6140.1–6494.1	6286.6 ± 2.2	128.2 ± 2.0	6300.7	112.5	0.83	6238.5	25.4	0.17	0.104
	1997/04/02	6165.2–6468.4	6288.5 ± 3.6	123.7 ± 6.0	6299.5	112.2	0.86	6241.8	19.9	0.14	0.090
	1997/05/14	6143.0–6508.3	6291.5 ± 2.2	126.0 ± 1.0	6302.1	114.2	0.87	6240.8	19.6	0.13	0.073
1997B	1997/09/23	6186.0–6438.9	6301.0 ± 8.6	110.7 ± 10.0	6295.5	93.6	0.63	6317.7	143.0	0.37	1.011
	1997/10/11	6206.4–6432.3	6296.7 ± 7.7	96.2 ± 15.0	6280.6	83.1	0.56	6318.8	86.0	0.44	1.048
	1998/02/02	6201.3–6481.6	6304.6 ± 5.9	97.3 ± 15.0	6286.3	71.1	0.37	6318.4	95.2	0.63	0.968
1997X	1997/05/10	6156.4–6495.1	6295.8 ± 2.2	106.3 ± 4.0	6298.4	146.5	0.53	6294.7	77.0	0.47	0.693
	1997/05/13	6143.4–6517.7	6297.2 ± 1.5	122.6 ± 3.0	6295.3	145.3	0.76	6300.2	72.2	0.24	0.566
1997dq	1998/05/30	6205.0–6446.5	6300.0 ± 2.8	97.8 ± 1.0	6323.7	68.7	0.55	6271.2	63.6	0.45	0.592
	1998/06/18	6202.2–6439.8	6298.8 ± 4.0	98.6 ± 7.0	6320.5	71.5	0.55	6270.2	72.7	0.45	0.840
1997ef	1998/09/21	6166.1–6470.1	6294.9 ± 5.3	120.2 ± 15.0	6300.6	179.2	0.72	6290.8	44.8	0.28	0.486
1998bw	1998/09/12	6090.0–6549.7	6298.4 ± 5.8	185.5 ± 6.0	6297.3	191.2	0.97	6315.1	31.6	0.03	0.730
	1998/11/26	6135.6–6504.6	6298.4 ± 3.2	146.1 ± 4.0	6292.8	166.1	0.87	6315.1	42.6	0.13	0.124
	1999/04/12	6134.6–6500.3	6299.3 ± 3.4	120.6 ± 5.0	6294.0	142.8	0.84	6310.8	39.1	0.16	0.107
	1999/05/21	6162.3–6460.7	6297.6 ± 3.2	109.8 ± 3.0	6291.7	132.7	0.82	6308.2	39.0	0.18	0.163
1999cn	2000/08/04	6198.2–6421.9	6294.6 ± 10.3	108.4 ± 20.0	6292.0	123.0	0.96	6303.7	32.9	0.04	0.785
1999dn	2000/09/01	6214.1–6455.2	6309.6 ± 10.2	94.3 ± 20.0	6304.1	112.9	0.81	6322.9	33.8	0.19	0.920

Table A1. *cont.* Parameters^a of the best one-component (cols. 4–5) and two-component (cols. 6–12) fits of [O I] λ 6300 – 2nd part.

SN (1)	Date (2)	Sample region (3)	λ (4)	FWHM (5)	λ_1 (6)	FWHM ₁ (7)	α_1 (8)	λ_2 (9)	FWHM ₂ (10)	α_2 (11)	rel. RMS ^b (12)
2000ew	2001/03/17	6189.4–6420.2	6284.3 ± 3.0	99.3 ± 5.0	6294.3	109.6	0.79	6266.3	33.0	0.21	0.496
2002ap	2002/08/06	6082.7–6529.4	6297.9 ± 2.3	172.5 ± 5.0	6296.6	179.2	0.96	6312.3	21.9	0.04	0.615
	2002/06/17	6064.6–6516.5	6300.0 ± 1.5	174.0 ± 3.0	6298.7	181.5	0.95	6312.5	22.5	0.05	0.254
	2002/07/11	6084.1–6514.9	6302.4 ± 1.5	163.1 ± 1.0	6301.6	164.6	0.97	6313.0	20.0	0.03	0.324
	2002/08/09	6103.9–6503.4	6304.6 ± 1.5	157.5 ± 1.0	6303.5	165.7	0.96	6314.1	21.6	0.04	0.164
	2002/10/01	6094.6–6513.3	6305.4 ± 1.5	150.4 ± 2.0	6304.1	157.9	0.95	6314.4	20.2	0.05	0.216
	2002/10/09	6104.7–6511.7	6305.0 ± 1.5	152.2 ± 4.0	6303.9	160.6	0.95	6313.5	20.3	0.05	0.366
	2002/10/14	6104.0–6511.2	6306.4 ± 1.5	153.9 ± 3.0	6304.2	166.4	0.93	6316.2	31.0	0.07	0.435
	2002/11/06	6149.5–6500.5	6305.7 ± 1.5	149.0 ± 1.0	6304.7	157.8	0.95	6312.5	22.2	0.05	0.247
	2003/01/07	6137.7–6519.0	6306.9 ± 2.3	143.0 ± 2.0	6305.9	150.8	0.95	6313.7	21.7	0.05	0.373
	2003/02/27	6145.0–6490.0	6309.5 ± 1.5	140.0 ± 2.0	6309.0	140.8	0.97	6315.4	17.1	0.03	0.534
2003jd	2004/09/11	6087.3–6505.8	6299.1 ± 3.6	219.6 ± 8.0	6232.0	116.7	0.50	6357.2	87.0	0.50	0.435
	2004/10/18	6150.7–6488.2	6304.4 ± 6.3	187.5 ± 15.0	6251.4	87.0	0.52	6358.5	67.8	0.48	0.584
2004aw	2004/11/14	6124.1–6498.6	6296.1 ± 3.3	118.7 ± 7.0	6293.1	133.0	0.89	6307.6	37.0	0.11	0.507
	2004/12/08	6191.6–6430.1	6289.2 ± 6.6	91.0 ± 14.0	6287.5	94.7	0.94	6302.9	34.8	0.06	0.882
	2005/05/11	6199.0–6442.0	6298.0 ± 6.6	91.4 ± 16.0	6294.0	101.8	0.87	6310.8	32.7	0.13	0.651
2004gt	2005/05/24	6174.8–6485.3	6285.2 ± 3.1	125.1 ± 3.0	6260.7	72.5	0.60	6335.8	87.1	0.40	0.490
2005N	2005/01/21	6160.0–6476.3	6268.6 ± 6.5	117.3 ± 7.5	6284.0	126.3	0.77	6241.2	46.8	0.23	0.353
2006F	2006/11/16	6223.0–6450.9	6296.9 ± 6.3	75.8 ± 20.0	6314.6	84.7	0.64	6281.4	38.9	0.36	0.508
2006T	2007/02/18	6203.0–6452.4	6300.5 ± 8.0	123.6 ± 16.0	6266.8	50.7	0.51	6338.0	57.9	0.49	0.306
2006aj	2006/09/19	6101.0–6498.7	6294.6 ± 6.1	188.5 ± 9.0	6295.0	192.2	0.99	6301.8	18.1	0.01	0.891
	2006/11/27	6096.0–6515.7	6303.5 ± 6.7	203.4 ± 11.0	6304.5	222.4	0.93	6300.8	35.3	0.07	0.588
	2006/12/19	6119.2–6507.0	6305.2 ± 7.7	177.1 ± 12.0	6306.2	197.4	0.92	6302.3	22.4	0.08	0.410
2006gi	2007/02/10	6138.3–6433.0	6278.5 ± 4.0	107.0 ± 2.0	6280.1	114.5	0.93	6267.7	35.2	0.07	0.458
2006ld	2007/07/17	6176.4–6492.5	6285.5 ± 2.2	97.2 ± 5.5	6304.8	104.0	0.70	6259.7	43.9	0.30	0.572
	2007/08/06	6173.5–6491.2	6287.6 ± 3.1	102.1 ± 9.0	6305.7	115.1	0.72	6263.5	43.8	0.28	0.531
	2007/08/20	6175.5–6482.4	6290.3 ± 2.6	92.7 ± 7.0	6296.3	87.3	0.89	6251.9	33.9	0.11	0.936
2007C	2007/05/17	6131.0–6501.4	6278.2 ± 3.6	122.5 ± 2.0	6301.1	92.3	0.69	6235.0	52.4	0.31	0.446
	2007/06/20	6134.0–6502.5	6285.3 ± 2.6	121.5 ± 1.5	6299.6	103.2	0.81	6237.6	41.6	0.19	0.344
2007I	2007/06/18	6157.1–6494.7	6300.3 ± 5.3	118.8 ± 1.0	6305.3	126.1	0.90	6277.8	35.8	0.10	0.122
	2007/07/15	6159.2–6504.8	6303.4 ± 5.3	111.9 ± 1.5	6308.2	116.3	0.90	6278.8	33.7	0.10	0.129

^a Central wavelengths (λ_i), full widths at half maximum (FWHM_{*i*}) and relative strengths (α_i) of the fit components (cf. Section 3.2). The sample region, λ and FWHM are given in units of Å.

^b RMS of the fit, relative to the RMS of the one-component fit.

^c The fitting was performed in H α -subtracted spectra. For this purpose, a smoothed symmetric H α profile was subtracted, constructed by reflecting the red wing at the rest wavelength (see also Patat et al. 1995).

Table A2. Parameters^a of the best three-component fits of [O I] λ 6300 for selected spectra with complex line profiles or particular geometric configurations.

SN (1)	Date (2)	Sample region (3)	λ_1 (4)	FWHM ₁ (5)	α_1 (6)	λ_2 (7)	FWHM ₂ (8)	α_2 (9)	λ_3 (10)	FWHM ₃ (11)	α_3 (12)	RMS ^b (13)	Config. (14)
1990B	1990/04/18	6132.1–6499.7	6319.9	180.7	0.71	6235.5	50.0	0.26	6303.1	13.0	0.03	0.140	clumpy
1997dq	1998/05/30	6205.0–6446.5	6272.4	63.3	0.49	6326.9	63.3	0.49	6298.4	12.3	0.02	0.480	DP + NC
1998bw	1999/05/21	6162.3–6460.7	6259.4	118.2	0.38	6319.4	118.2	0.38	6307.8	45.0	0.24	0.175	DP + NC
2002ap	2002/10/01	6094.6–6513.3	6251.8	102.6	0.42	6352.1	102.6	0.42	6313.5	42.3	0.15	0.170	DP + NC
2004gt	2005/05/24	6174.8–6485.3	6243.8	63.7	0.37	6338.6	63.7	0.37	6279.3	44.3	0.26	0.229	DP + blob
2006aj	2006/12/19	6119.2–6507.0	6256.9	151.4	0.45	6353.3	151.4	0.45	6302.2	24.1	0.09	0.402	DP + NC
2006ld	2007/07/17	6176.4–6492.5	6320.8	121.4	0.48	6261.6	40.1	0.40	6301.6	20.0	0.12	0.161	clumpy
	2007/08/06	6173.5–6491.2	6320.4	136.6	0.53	6264.2	39.4	0.36	6302.1	21.1	0.11	0.212	clumpy
	2007/08/20	6175.5–6482.4	6322.3	117.5	0.47	6264.4	46.5	0.37	6303.2	19.9	0.16	0.343	clumpy
2007C	2007/05/17	6131.0–6501.4	6299.0	127.1	0.56	6239.5	54.2	0.29	6301.1	43.1	0.15	0.088	NC + blob
	2007/06/20	6134.0–6502.5	6297.7	125.6	0.68	6242.0	43.5	0.19	6304.4	41.4	0.13	0.060	NC + blob

^a Central wavelengths (λ_i), full widths at half maximum (FWHM_{*i*}) and relative strengths (α_i) of the fit components (cf. Section 3.2). The sample region, λ and FWHM are given in units of Å.

^b RMS of the fit, relative to the RMS of the one-component fit (cf. Table A1).